ESTIMATE HOURLY AND DAILY EVAPOTRANSPIRATION USING REMOTE SENSING TECHNOLOGY FOR HAIHE RIVER BASIN

JING ZHAO
Feb, 2017

SUPERVISORS:
Dr. X. Chen
Prof. Dr. Z. Su

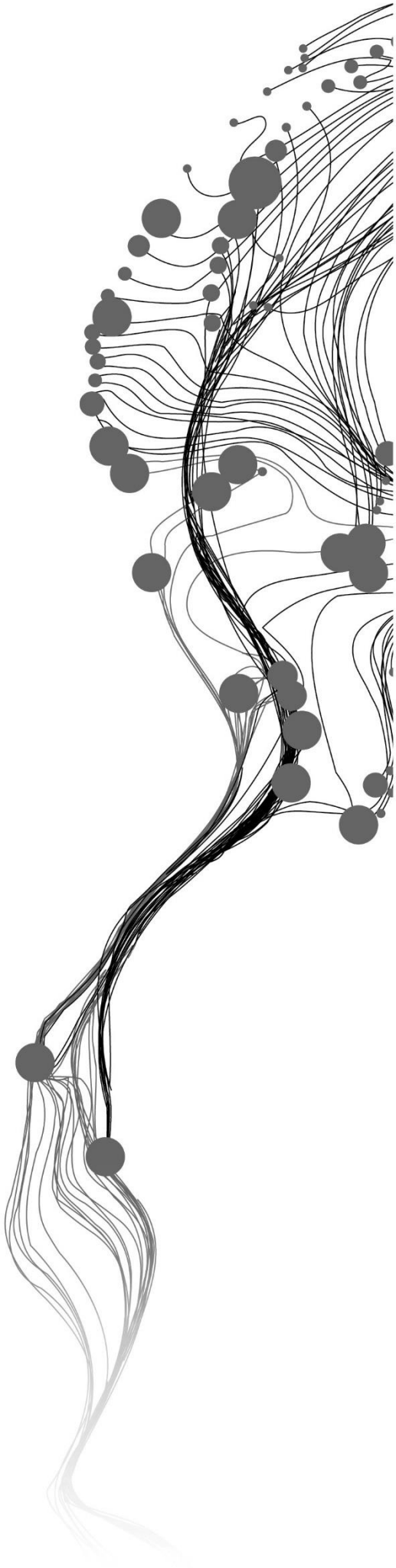

ESTIMATE HOURLY AND DAILY EVAPOTRANSPIRATION USING REMOTE SENSING TECHNOLOGY FOR HAIHE RIVER BASIN

JING ZHAO
Enschede, The Netherlands, [February, 2017]

Thesis submitted to the Faculty of Geo-Information Science and Earth Observation of the University of Twente in partial fulfilment of the requirements for the degree of Master of Science in Geo-information Science and Earth Observation.
Specialization: [Water Resource and Environmental Management]

SUPERVISORS:
Dr. X. Chen
Prof. Dr. Z. Su

THESIS ASSESSMENT BOARD:
Dr. M.W. Lubczynski (Chair)
Dr. Yaping, Liu (External Examiner, Capital Normal University)

ABSTRACT

Evapotranspiration (ET) is one of the key variables in hydrological cycle, it is a term used to describe the combined loss of water due to evaporation from soil surfaces and transpiration from plants. Therefore, the research of evapotranspiration has a great significance for understanding climate change and the impacts of climate change on water resource management.

Haihe River basin is distinct on the conflict of water resource and water environment in China; This basin is China's important industrial base, high-tech industrial base and one of the three major grain production bases. But this area has serious problems of shortage of water resources, water pollution and the ecological environment deterioration.

This study estimated hourly and daily evapotranspiration using SEBS (surface energy balance system) model with Geo-stational remote sensing data and available meteorological observations. It is a single layer model for estimation of regional evapotranspiration with high precision based on the surface energy balance, which can calculate net radiation, ground heat flux as well as sensible heat flux, and then, get the latent heat flux and evapotranspiration. This study utilized the SEBS model over Haihe River Basin, combined with some new parameterization updated method.

The paper analysis the surface characteristic parameters from MTSAT and ITPCAS meteorological forcing data sets. Both of them are in highest temporal and spatial scale among current available land surface research datasets. Due to difference in spatial and temporal resolution of the two-forcing dataset, a pre-processing has been done with the two datasets to match their temporal and spatial distribution in the study area. Analysis of land surface radiation, water and heat flux and evapotranspiration from SEBS model were done by the thesis. Five flux tower measurements located in the basin were collected during the field work. The high quality of the ground observations was then used to validates the model result and analyze the error at flux tower point. The results show that, the root square R^2 (the coefficient of determination) of evapotranspiration is equal to 0.67 indicateding hourly and daily evapotranspiration derived from SEBS model performed well in the study area. The estimation for high temporal resolution evapotranspiration using remote sensing method is feasible. Finally, the influence factor for SEBS evapotranspiration and possible error sources were also pointed out based on the result of this study.

Key works: Evapotranspiration; MTSAT; SEBS model; Hiahe River Basin; High temporal resolution

ACKNOWLEDGEMENTS

I would like to express my gratitude to all those who helped me during the writing of this thesis.

My deepest gratitude goes first and foremost to Dr. Xuelong Chen, my first supervisor, for his constant encouragement and guidance. He has walked me through all the stages of the writing of this thesis. Without his consistent and illuminating instruction, this thesis could not have reached its present form.

I would like to extend my sincere gratitude to my second supervisor, Professor. Bob Su, for his instructive advice and useful suggestions on my thesis. I am deeply grateful of her help in the completion of this thesis.

Last my thanks would go to my beloved family for their loving, considerations and great confidence in me all through these years. I also owe my sincere gratitude to my friends and my fellow classmates who gave me their help and time in listening to me and helping me work out my problems during the difficult course of the thesis.

TABLE OF CONTENTS

LIST OF FIGURES

LIST OF TABLES

LIST OF ABBREVIATION

ABL	Atmospheric Boundary Layer
EC	Eddy Covariance
ET	Evapotranspiration
G_0	Ground heat flux
H	Sensible heat flux
HC	Canopy height
IGBP	International Geosphere Biosphere Programme
LAI	Leaf Area Index
LE	Latent heat flux
LST	Land Surface Temperature
LWD	Downward longwave radiation
LWU	Upward longwave radiation
MODIS	Moderate Resolution Imaging Spectro radiometer
MTSAT	Multifunctional Transport Satellites
NDVI	Normalized Difference Vegetation Index
ITPCAS	The Institute of Tibetan Plateau Research, Chinese Academy of Sciences
P	Precipitation
PBL	Planetary Boundary Layer
RMSE	Root Mean Square Error
SEBS	Surface Energy Balance System
SWD	Downward shortwave radiation
SWU	Upward shortwave radiation

1. INTRODUCTION

1.1. Background

Since the 20st century, water resource issues are increasingly affecting the global environment and economic development. China is a large country, covering a land area of about 9.6 million square kilometres. Uneven distribution of water resources, flood and drought disasters occur frequently in China. These natural disasters have a direct impact on water resource management in a river basin. For example, in the karst regions of South China, water resources were scarcity in most provinces during 2000–2013 (L. Wan, Zhou, Guo, Cui, & Liu, 2016). In this region, frequent drought occurrences have effects on the availability of water resources and have consequently caused increasing risks of water-related stresses to human's living.

In environmental systems, hydrological cycle is directly linking atmospheric processes and land surface processes (Chahine, 1992; Sellers et al., 1997). Therefore, the development of agriculture, ecology and social economy is closely related to the impact of water resources. Some researchers assess the impacts of projected climate change on water availability and crop production in the Volta Basin and the southwestern and coastal basin systems of Ghana (Amisigo, McCluskey, & Swanson, 2015). Quantifying the consumption of water over large areas and irrigated farmland is important for water rights management, water resources planning, hydrologic water balances, as well as water regulation (Howell, 2001).

Evapotranspiration (ET) is one of the key variables in hydrological cycle, it is a term used to describe the combined loss of water due to evaporation from soil surfaces and transpiration from plants. ET is a central process in the climate system and a nexus of the water, energy and carbon cycles (Jung et al., 2010). Therefore, the research of evapotranspiration has a great significance for understanding climate change and the impacts of climate change on water resource management. The instruments are expensive, meanwhile they provide us ET observation at points. This limits our knowledge on ET spatial-temporal variation.

Spatial estimates of ET are essential components of general circulation and hydrologic models. There are many methods to measure ET from either ground observation or remote sensing satellite data. Typically, ground observation, e.g. lysimeters, bowen ratio systems, eddy covariance (EC) systems, requires advanced instrumentation and a high level of data screening and interpretation (Bhantana & Lazarovitch, 2010).

Recently, with the development of remote sensing (RS) and geographic information systems (GIS), we can model and simulate the evapotranspiration process by remote sensing methods(Abtew & Melesse, 2013). Currently, there are many methods have been developed, such as SEBAL (Bastiaanssen et al., 1998), TSEB(Norman & Becker, 1995), and SEBS (Su, 2002). For example, Ma et al. (2013) deals with the application of SEBS based on ASTER data and field observations, Wu et al. (2016) estimate daily surface resistance using a Penman–Monteith (P–M) formulation, and Allen et al. (2007) map evapotranspiration using high resolution with the internalized calibration (METRIC) model which is a satellite image-processing model.

In these evapotranspiration models, land surface parameters play a crucial role for the better estimation of evapotranspiration. These models also require explicit characterization of numerous physical parameters, however, many of them are difficult to determine. High temporal and spatial resolution satellite image can reduce the uncertainty of input parameters. In addition, most of remote sensing ET calculation used high spatial resolution satellite data, e.g. Landsat (Table 1-1), MODIS (Table 1-2), ASTER (Ma et al., 2013). However, the disadvantages of using these to diagnostic modelling in above papers with these specific sensors is that the output records often suffer from large spatial and temporal gaps due to cloud cover and infrequent image availability as governed by the satellite overpass schedule. Therefore, more effort should be given to the generation of a more robust product. Geostationary satellite has a high temporal resolution, it can provide us with hourly and daily land surface information, which gives us a high potential to calculate land surface and water cycle at hourly temporal resolution. Therefore, we can use geostationary satellite data as input parameter to calculate evapotranspiration. However, there are few work on ET remote sensing retrieval using Geo-stational satellite data. For example, Mamo (2010) using ground meteorological station, and combined high temporal resolution geostationary satellite products and relatively high spatial resolution polar orbiting satellite products to estimate daily actual evapotranspiration of Spain.

Thus, it should be possible to use geostationary satellite data and ground-based meteorological data to calculate hourly and daily evapotranspiration in my study area. This study focuses on making use of MTSAT geostationary satellite data; combining with metrological data for estimation of hourly actual evapotranspiration. In addition, comparison will be taken between SEBS remote sensing ET and ground observed ET.

Table 1-1 Main characteristics of LANDSAT 8 OLI

Band	Band name	Wavelength/μm	Spatial resolution	Temporal resolution
1	Coastal	0.433–0.453	30 m	16 day
2	Blue	0.450–0.515	30 m	16 day
3	Green	0.525–0.600	30 m	16 day
4	Red	0.630–0.680	30 m	16 day
5	NIR	0.845–0.885	30 m	16 day
6	SWIR 1	1.560–1.660	30 m	16 day
7	SWIR 2	2.100–2.300	30 m	16 day
8	Pan	0.500–0.680	15 m	16 day
9	Cirrus	1.360–1.390	30 m	16 day
10	TIRS	10.60-11.19	100 m	16 day
11	TIRS	11.50-12.51	100 m	16 day

Table 1-2 MODIS/Terra land surface reflectance products

Product	Name	Spatial resolution	Temporal resolution
MOD09GA	Surface Reflectance Bands 1–7	500/1000m	Daily
MOD09GQ	Surface Reflectance Bands 1–2	250m	Daily
MOD09CMG	Surface Reflectance Bands 1–7	5600m	Daily
MOD09A1	Surface Reflectance Bands 1–7	500m	8 Day
MOD09Q1	Surface Reflectance Bands 1–2	250m	8 Day

1.2. Problem Statement

Water resource is a decisive factor restricting economic development and ecological restoration, also is the core issue of the environment and ecosystem research in arid areas. Evapotranspiration is most important part of water cycle in arid inland. It plays a crucial role in water cycle research, agricultural water saving, the water resources management and drought monitoring.

Haihe River basin is China's important industrial base, high-tech industrial base and one of the three major grain production bases. But this area has serious problems of shortage of water resources, water pollution and the ecological environment deterioration. Furthermore, the estimation of evapotranspiration becomes difficult in this area because of its complicated underlying surface conditions. Therefore, there is an urgent need for knowledge of the basin water balance items and its spatial distribution and temporal changes with scientific and quantitative understanding. However, the previous studies about actual evapotranspiration mostly focus on annual, monthly or selected ET on specific date (Bhattarai, Shaw, Quackenbush, Im, & Niraula, 2016; Ma et al., 2013; Rwasoka, Gumindoga, & Gwenzi, 2011; Wang, Li, & Tang, 2013). Therefore, this study aims to improve temporal resolution to hourly and daily evapotranspiration using MTSAT meteorological satellite. By this means, spatial and temporal distribution of water and energy within this catchment can be obtained, also can further improve the research achievements of water and weather, promote the rational use of water resources, and provide basic data for the Haihe River basin water resource management.

1.3. Objectives and research questions

1.3.1. General objective

The general objective of this research is to estimate actual hourly and daily evapotranspiration using remote sensing technology and meteorological forcing dataset in Haihe River basin.

1.3.2. Specific objectives

The specific objectives are:

1. Quantification of hourly and daily evapotranspiration (ET) using SEBS model (surface energy balance system) and Geo-stational thermal remote sensing for Haihe River scale
2. Comparison of estimated ET and in-situ measured ET
3. To investigate the role of model input parameters/variables derived from geo-stationary satellite, to the ET accuracy.

1.3.3. Research questions

These objectives aim to answer these research questions:

1. What is the advantage of using MTSAT geo-stationary satellite data to estimate actual evapotranspiration?
2. It is possible to use SEBS model to estimate hourly/daily ET?
3. What is the problem in SEBS parameterized method for the study area?
4. What is the spatial and temporal variation of ET products for Haihe River basin?
5. How was the accuracy of hourly/daily ET and its uncertainty sources?

1.4. Thesis outline

This thesis consists of seven chapters.

Chapter 1 provides an introduction of this study, the problem definition, research objectives and questions. Chapter 2 gives a literature review on evapotranspiration and its physical background followed by several estimation approaches of ET, focusing on the research status of SEBS algorithm in terms of estimating ET. Chapter 3 provides a description of study area and data collection from fieldwork. Chapter 4 contains an introduction of data sets used for this research work, as well as the pro-processing of satellite images and meteorological data. Chapter 5 discusses the SEBS model followed by its application in this study area. Chapter 6 gives the results of spatial and temporal variation of ET with time series and discussion, including the evaluation of influence factor (land use, vegetation, and climate). Chapter 7 provides a conclusion and few recommendations.

2. LITERATURE REVIEW

2.1. Evapotranspiration

Evaporation refers to the process of water from liquid to gaseous. Transpiration is the emission of water vapour from the plants. Evapotranspiration (ET) is the sum of transpiration and evaporation from land surface, include free water surface evaporation, land surface evaporation and plant transpiration. In contrast with precipitation, evapotranspiration is a process that transfers water from the ground to atmosphere (Thornthwaite, 1948). It is a core process in climate system, closely links hydrological cycle, carbon cycle and energy balance (Jung et al., 2010).

2.1.1. Reference evapotranspiration (ET_0)

In order to facilitate the research and calculation, the reference evapotranspiration has been put forward assuming the vegetation condition is under the condition of sufficient water supply. It is also called reference crop evapotranspiration which evaporation and transpiration from short, well-watered grass or open water.

The concept of the reference evapotranspiration can be used to do research about evaporative demand of crop type, crop development and management practices. As water is abundantly available at the reference surface, soil factors do not affect ET. ET_0 can be computed from meteorological data and from pan evaporation

2.1.2. Potential evapotranspiration (ET_c)

Potential evapotranspiration can be generally defined as the amount of water that could evaporate and transpire from a vegetated landscape with sufficient water supply of the underlying surface (Penman, 1948; Thornthwaite, 1948). The potential evapotranspiration is the ability of the underlying surface evapotranspiration, which is the theoretical upper limit of actual evapotranspiration. This evapotranspiration data can be used to calculate the water requirements of crops and landscape plants, adjust irrigation schedules in a way that encourages efficient water use, reduces waste as well as saves money. Potential evapotranspiration is generally estimated by three methods: temperature method, radiation method and synthesis method (Hargreaves & Samani, 1982; Holdridge, 1959; Penman, 1948; Thornthwaite, 1948).

2.1.3. Actual evapotranspiration (ET_a)

Actual evapotranspiration is the sum of evaporation from ground surface and transpiration from vegetation in the actual soil moisture condition. The actual evapotranspiration is a problem of evaporation under natural conditions, which is not only affected by meteorological factors such as energy balance, poor saturation, air temperature, but also affected by the factors of the underlying surface. For example, evaporation from soil is not only related to atmospheric conditions, but also with the soil factors. Another example is the transpiration from vegetation, is related to vegetation type and growth status.

2.2. Estimating actual evapotranspiration

The theory of evaporation calculation proposed by Dalton in 1802 provides a strong theoretical basis for near-contemporary researches of evapotranspiration. For either traditional or the remote sensing ET estimating method, the theoretical basis is the same. Most of the method uses energy surface balance equation. It describes the heat and water transfer from different source to land surface with:

$$R_n = G_0 + H + \lambda E \tag{2-1}$$

where R_n is the net surface radiation, G_0 is the soil heat flux, H is the turbulent sensible heat flux, and λE is the turbulent latent heat flux (λ is the latent heat of vaporization equal to 2.49×10^6 J/kg and E is the actual evapotranspiration).

With the significant progress in ET research, many estimation method of evapotranspiration has innovated, such as gradient method, bowen ratio method, eddy covariance method, Penman – Monteith method, and lysimeter method.

Recently, Malamos et al. (2015) estimate monthly evapotranspiration of Western Greece using Penman – Monteith method. In addition, Uddin et al. (2013) proposed a precision energy budget (Bowen ratio and eddy covariance method) to measure latent heat flux in the University of Southern Queensland. This research combined these two methods, and concluded that EC (eddy covariance)-based technique can able to measure the different rate of evapotranspiration over short crop during sprinkler irrigation. Effort have been undertaken by Migliaccio (2014) as well to estimate evapotranspiration using the eddy covariance method and crop coefficient (K_c). The results show that their new K_c values are more suitable for South Florida Water Management District canal.

2.3. Remote sensing of evapotranspiration

The traditional ground measurement has difficult to meet the demand of regional evapotranspiration distribution studies. The remote sensing technique can provide support for estimating evapotranspiration and application development in a regional scale, especially in a basin scale. Remote sensing data can provide net radiation and the impedance surface parameters. Therefore, some studies estimate actual evapotranspiration by traditional method in combination with remote sensing(Baik & Choi, 2015; Tsouni, Kontoes, Koutsoyiannis, & Elias, 2008; Yao et al., 2013). Cleugh et al. (2007) estimate evapotranspiration for Australia using surface energy system model and Penman-Monteith equation.

Recently, most remote sensing methods use evapotranspiration model based on surface energy balance as indicated before. Classical evapotranspiration model include SEBAL (Bastiaanssen et al., 1998) model and SEBS(Su, 2002), they are single source model which consider soil and plant as sole source. In addition, dual source (soil and canopy of vegetation are treat separately) model, e.g. TSEB (Norman & Becker, 1995), SEBI (Menenti & Choudhury, 1993)and ALEXI model (Anderson, Norman, Diak, Kustas, & Mecikalski, 1997), were also developed by scientists.

Remote sensing data can be used to solve the challenges of our needs for space distribution. It can observe a series of physical properties on the earth's surface regularly; these properties can be used to

estimate evapotranspiration by using a parameterization method in a regional scale. Remote sensing tech measuring thermal infrared, infrared and visible wavelengths data can serve for parameters retrievals for energy balance and ET calculation.

2.4. Review on MTSAT satellite

Land surface temperature (LST) is an important parameter which represents the processes of energy and water exchange. This means that this variable determining the upward thermal radiation and affecting the heat exchange from Earth's surface to atmosphere. It can be retrieved from thermal infrared radiation sensors. MTSAT, a Japanese geostationary meteorological satellite, can provide some land surface parameters for Haihe River Basin. Surface solar irradiance estimates have been made by Huang et al. (2011) using MODIS and MTSAT data. Their research combining two kinds of data to capture the changes of cloud field in the atmosphere and obtain land surface parameters such as water vapour, surface reflectance. Split-window method can be used to retrieval land surface temperature from meteorological satellite data (Becker & Li, 1990). Effort have been undertaken by Kim et al. (2011) and (Oyoshi, Akatsuka, Takeuchi, & Sobue, 2015)as well to develop land surface temperature by split-window algorithm. They applied this method to MTSAT-2 data for the continuous retrieval of land surface temperature. In addition, MTSAT data also can be used to hourly sea surface temperature retrieval (Cho, Ho, & Choi, 2012; Kawamura, Qin, Sakaida, & Setiawan, 2010; M. J. Kim, Ou, Sohn, & Kim, 2011)

3. STUDY AREA AND DATA COLLECTION

3.1. Study area

3.1.1. Location

Haihe River basin is a drought-prone region, plays an important role in the sustainable development of the economy and ecology of China. It located in the north of China; geographical coordinate is between 35°N – 41.5°N, 112°E – 118.5°E (Figure 3-1). The watershed covers an area of 318,200 km², accounting for 3.5 percent of the total area of China.

The upper, middle and lower reaches of this river basin stretch from north Henan Province to southern Inner Mongolia, consists of three major river systems: the Luan River, Haihe River and Majia River. It cover the entire areas of Beijing and Tianjin Municipalities, most of the area of Hebei Province, and partial areas of Shandong Province, Henan Province, Shanxi Province, the Inner-Mongolia Autonomous Region and Liaoning Province (Y. Jia et al., 2009).

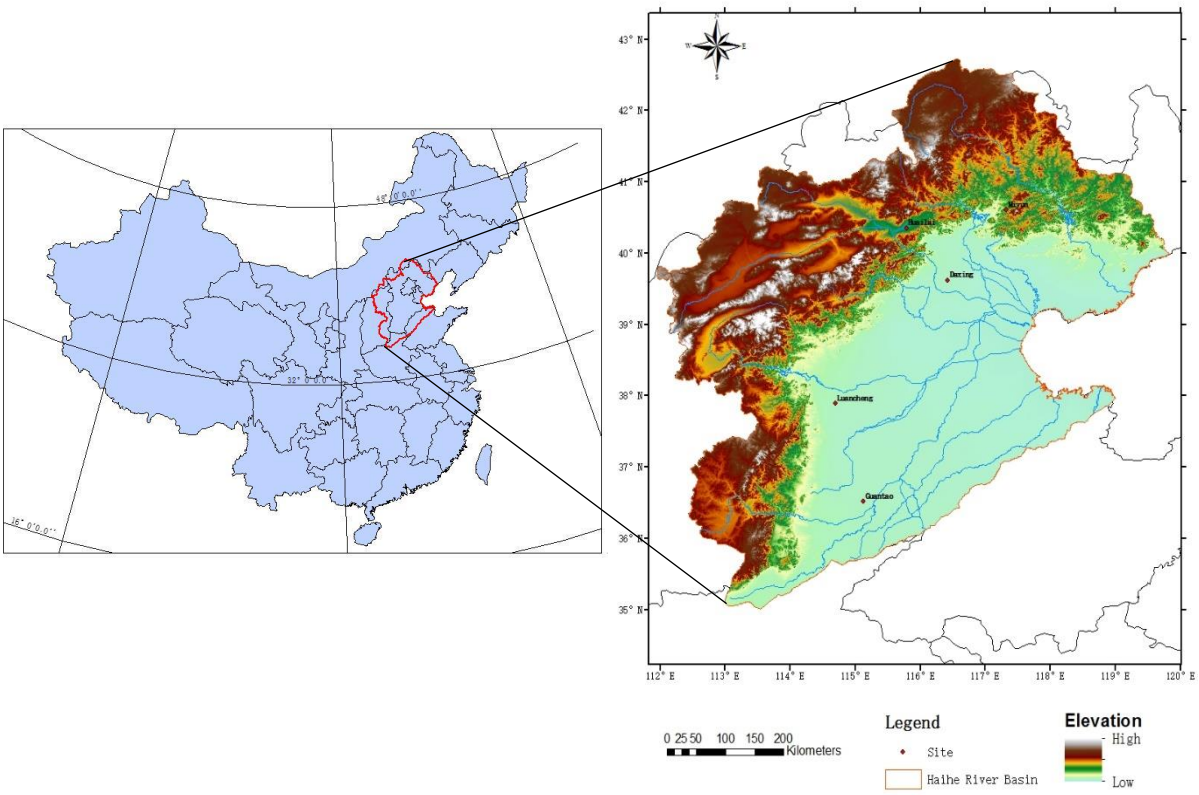

Figure 3-1 The location and elevation of Haihe River basin

3.1.2. Topography

The general topography in Haihe River is high in northwest, low in southeast. It can be divided into three kinds of landforms: plateau, mountains and plains. In the western part of Haihe River basin is loess plateau of Shanxi and Taihang Mountain, which are mountainous area and the elevation is among 1200-2000 m. In the northern part of the basin is Mongol highland and Yanshan Mountain. The runoff is generated mainly from these two parts and is the source of the surface water and groundwater. Eastern and south-eastern of Haihe River is vast plain, which is the agricultural region and a lot of surface water is consumed here for irrigation.

3.1.3. Climate

Haihe River Basin connects with Bohai Bay, belongs to temperate semiarid continental monsoon climate, northerly and north-westerly winds prevail in winter, while southerly winds reign in summer. The annual average temperature of this area is 1.5 to 14 °C; mean average humidity is 50 to 70 %. In this region, the average annual precipitation is 530 mm with approximately 80% of rainfall occurring from June through September (Guo & Shen, 2015) and potential evapotranspiration of 960 mm during 1961-2010 (Shaohua Liu et al., 2016).

3.1.4. Vegetation

The distribution of vegetation in Haihe River Basin has three parts: temperate grassland area in Inner Mongolia, temperate deciduous broad-leaved forest zone in the mountainous area of North China, warm-temperate deciduous broad-leaved forest and crop area in Haihe plain. Most of the natural vegetation in the Haihe River Basin has been destroyed by human deforestation, only a small amount of natural vegetation distributed in the mountains.

Figure 3-2 Landscape of Haihe River Basin (Photo was taken on October 2016 during fieldwork)

3.2. Fieldwork and data collection

For this study, fieldwork was taken between 14 October and 26 October, 2016. This fieldwork is carry out based on the research of hourly and daily evapotranspiration using remote sensing technology. The main objective of this field work is to collect the data required for the validation of ET and land cover product, including the flux tower data, meteorological data and other secondary data in Haihe River basin.

The fieldwork consisted of the following activities:

- Obtaining flux tower data
- Observation of flux site with exiting data
- Some information of land use and land cover in study area
- Collecting other useful data

In addition, some site (Miyun, Guantao and Daxing) data for validation and analysis were download from internet. The table (Table 3-1) shows the overview of measurement period for the five sites date used in this study.

Table 3-1 Measurement period of all site data used for product validation and analysis

Site Name	Measurement period			
	Meteorology (P)	Radiation (SWD, LWD, SWU, LWU)	Eddy covariance (H, LE)	Lysimeter (ET)
Miyun	-	2008.1-2010.12	2008.1-2010.12	-
Guantao	-	2008.1-2010.12	2008.1-2010.12	-
Daxing	-	2008.1-2010.12	2008.1-2010.12	-
Luancheng	2010.10-2015.12	2014.10-2015.3	2014.10-2015.3	2010 - 2014
Huailai	2013.1-2014.12	2013.1-2014.12	2013.1-2014.12	2013 - 2014

3.2.1. Flux tower data

The result of estimated hourly and daily evapotranspiration should be validated with in-situ measurement data ensure it is believable. The traditional energy balance method (such as eddy covariance) at flux sites is applied for assessing evapotranspiration products.

During the fieldwork, I went to Huailai and Luancheng site to colleting the flux tower data, and also went to Daxing site to collecting equipment information. Other flux tower data is downloaded from the WestDC (Shaomin Liu, Xu, Zhu, Jia, & Zhu, 2013). Tower flux data were collected from other towers in 2007–2010 over the Hai River Basin(Liu et al., 2013), namely the Miyun, Daxing and Guantao station. The position of these five stations are shown in Figure 3-1. The elevation of these station range from 3 to 26.66m. Landcover including maize, winter wheat and orchard. Each station observation system include observation data of eddy covariance, large aperture scintillometer (LAS) and automatic weather station(Z. Jia, Liu, Xu, Chen, & Zhu, 2012). The detailed information of these sites is shown in Table 3-2.

Table 3-2 Detailed information about flux tower

Site Name	Location	Land cover	Maximum Vegetation Height (m)	Type	Elevation (m)
Luancheng	7°53'21.7"N, 114°41'34.5"E	Maize Winter wheat	Maize: 2.2 Winter wheat: 0.7	CPEC200 Li7550	3
Huailai	40°20'55.9"N, 115°47'17.5"E	Maize Winter wheat	Maize: 2.2 Winter wheat: 0.7	Gill & Li7500	10
Daxing	39°37'16.7"N, 116°25'37.2"E	Maize Winter wheat Vegetable	Maize: 2.2 Winter wheat: 0.7 Vegetable: 0.5	Li7500 and CSAT3, Li-cor and Campbell	3
Miyun	40°37'50.82"N, 117°19'23.83"E	Orchard Maize	Orchard (plum/apple tree): 4 Maize: 2.2	Li7500 and CSAT3, Li-cor and Campbell	26.66
Guantao	36°30'54.1"N, 115°07'38.7"E	Maize Winter wheat Cotton	Maize: 2.2 Winter wheat: 0.7 Cotton: 1.2	Li7500 and CSAT3, Li-cor and Campbell	15.6

These instruments can provide observational data which can be used to validate the performance of the SEBS model, such as horizontal wind velocity, saturated vapour density, friction velocity, sensible heat flux, latent heat flux etc.

Figure 3-3 Eddy covariance system in Huailai (left) and Luancheng (right) station

3.2.2. Radiation data

As mentioned above, these experimental stations also have net radiometer instrument: named CNR4 warranted by Campbell Scientific, Inc. This instrument is a four-component net radiometer which can measures the energy balance between incoming and outgoing radiation (longwave as well as shortwave radiation). Each sensor is calibrated individually for optimal accuracy.

3.2.3. Precipitation

Precipitation data was collected for the rain gauge station within the catchment, Huailai and Luancheng station. Both stations are use TE525-Rain gauge to measure the precipitation (Figure 3-4). The distribution of rainfall is shown in Figure 3-5. It shows that the precipitation in this area mostly happens in summer (June to September).

Figure 3-4 Rain gauge in Luancheng (Left) and Huailai (Right) station

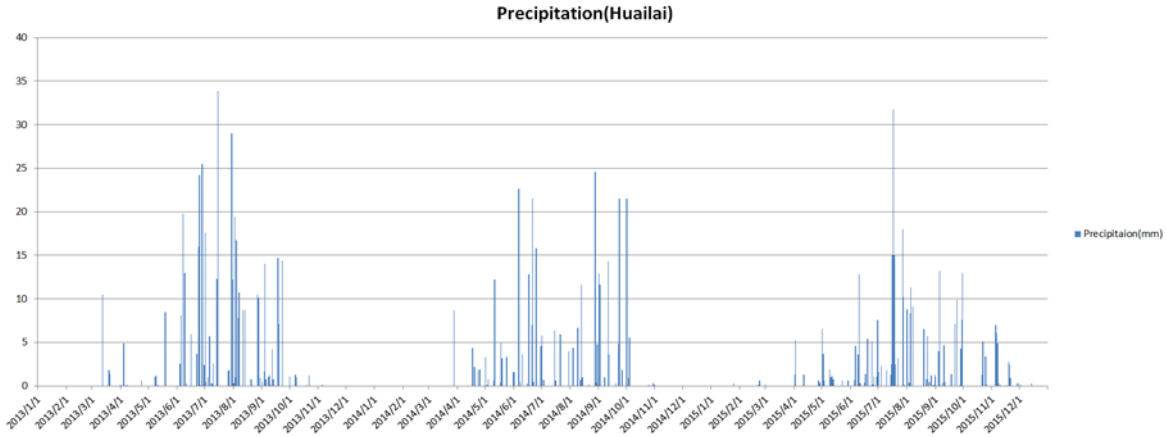

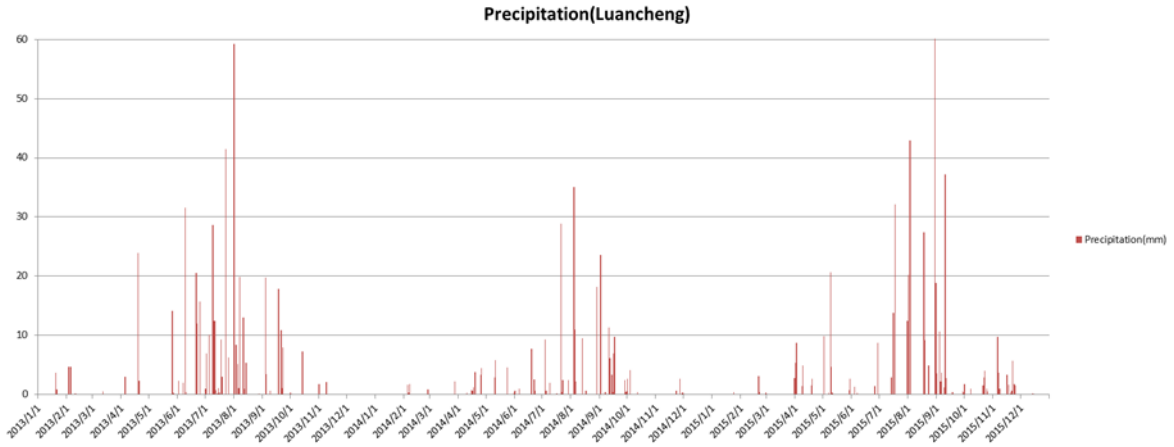

Figure 3-5 The distribution of rainfall in Haihe River Basin

3.2.4. Lysimeter

The lysimeter instrument is located in Luancheng station (37°53'22.0"N, 114°41'29.6"E). The farmland and the soil type is same as the local farmland, thus the data from this instrument can represent the character of this area. The same cultivation practices such as tillage depth, sowing date and seed number and varieties were applied to both the lysimeter site and its surrounding farmland (C. Liu, Zhang, & Zhang, 2002). This lysimeter has a steel box which area is 2.5 m × 2.5 m and the depth is 2 m. The precision of this lysimeter's weighting systems for measureing evapotranspiration is very high, can reach 0.017 mm (C. Liu et al., 2002). Therefore, it can be used to do the performance validation of hourly and daily evapotranspiration calculated by the SEBS model. The Figure 3-6 shown the distribution of daily ET measured by lysimeter in Luancheng site.

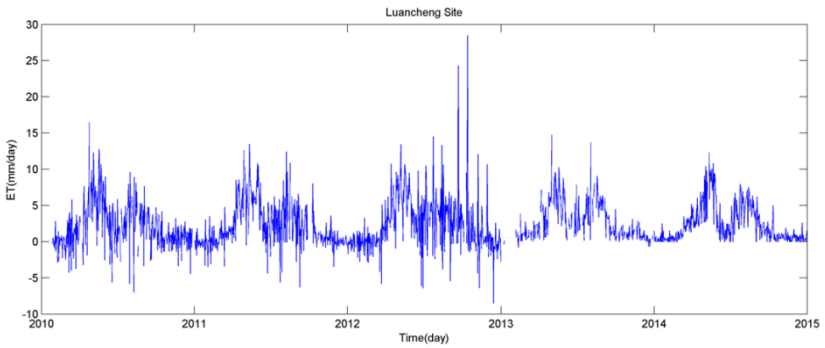

Figure 3-6 Distribution of ET by lysimeter in Luancheng site

4. SATELLITE DATA AND PRE-PROCESSING

4.1. Available data

4.1.1. MTSAT satellite data

The Multi-Functional Transport Satellite (MTSAT) series fulfils a meteorological function for the Japan Meteorological Agency and an aviation control function for the Civil Aviation Bureau (CAB) of the Ministry of Land, Infrastructure and Transport (MLIT). The MTSAT series succeeds the Geostationary Meteorological Satellite (GMS) series as the next generation of satellites covering East Asia and the Western Pacific. The images cover the Earth's surface from 5°N to 55°N and from 75° E to 145°E (Figure 4-1) (Wong et al., 2016), include most of Eastern Asia, Australia, New Zealand. The MTSAT series provides imagery for the Northern Hemisphere every 30 minutes. The series carries a new imager with a new infrared IR4 channel (3.5 ~ 4.0 μm) in addition to the four channels (VIS, IR1, IR2 and IR3) of the GMS-5 (Agency Japan Meteorological, 2008). The main characteristics of MTSAT series is shown in Table 4-1.

Figure 4-1 The coverage of MTSAT-1

Table 4-1 Main characteristics of MTSAT series

Channel	Wavelength/μm	Data quantization/bit	Pixel resolution/km
Visible light (VIS)	0.55 ~ 0.90	10	1
Infrared (IR1)	10.3 ~ 11.3	10	4
Infrared (IR2)	11.5 ~ 12.5	10	4
Infrared (IR3)	6.5 ~ 7.0	10	4
Infrared (IR4)	3.5 ~ 4.0	10	4

The MTSAT-1 successfully launched on February 18, 2006 and is an integral part of a next-generation global-scale air traffic safety system comprised of communications, navigation, tracking and air traffic control. The purpose is to improve traffic congestion and safety in the Asia Pacific region. Furthermore, it is designed to take on a meteorological mission to capture, collect and deliver meteorological images and/or data. In this capacity, it inherits and expands the mission of a previous satellite.

The MTSAT LST level-2 product used to this research is downloaded from GLOBTEMPERATURE project: GlobTemperature Data Portal (http://data.globtemperature.info/). It generalized Split-Window (GSW) algorithm and dual-algorithm from two adjacent TIR channels of MTSAT sensors to produce the LST, detailed information about the data processing can be found in Freitas et al. (2013). This data is available for the entire period of 2010-2014. Spatial resolution of the product is 0.5°, and temporal resolution is hourly (3-hourly before June 20th 2010).

4.1.2. Meteorological observation data

In order to use SEBS model to estimate ET, the standard meteorological information is required. Meteorological forcing data can be obtained from ground or numerical models. The China Meteorological Forcing Dataset (He & Yang, 2011) was used for this research. The new data set was developed by the hydro meteorological research group at the Institute of Tibetan Plateau Research, Chinese Academy of Sciences (ITPCAS). It is more accurate than other forcing data sets in calculating the energy flux according several research (X. Chen et al., 2014; Y. Chen et al., 2011; Xue et al., 2013; Kun Yang, He, Tang, Qin, & Cheng, 2010; Zhao et al., 2016). The meteorological forcing data was produced by merging a variety of data from ground observation and reanalysis. This dataset fuse CMA (China Meteorological Administration) 740 operational station data, TRMM satellite precipitation analysis data, GEWEX-SRB downward shortwave radiation, Princeton forcing data and GLDAS data. It currently covers the period of 1979-2015, spatial resolution is 0.1 degree and temporal resolution is 3 hours. The China Meteorological Forcing Dataset contains seven variables: temperature, pressure, specific humidity, wind speed, downward shortwave radiation, downward longwave radiation and precipitation rate (Table 4-2).

Table 4-2 Variables from The China Meteorological Forcing Dataset

Variables	Variables name	Unit	Physical meaning
Temperature	temp	K	Instantaneous near surface (2 m) air temperature.
Pressure	pres	Pa	Instantaneous near surface (2 m) air pressure.
Specific humidity	shum	kg/kg	Instantaneous near surface (2 m) air specific humidity.
Wind speed	wind	m/s	Instantaneous near surface (10 m) wind speed.
Downward shortwave radiation	srad	W/m^2	3-hourly mean (from -1.5 hr to +1.5 hr) surface downward shortwave radiation.
Downward longwave radiation	lrad	W/m^2	3-hourly mean (from -1.5 hr to +1.5 hr) surface downward longwave radiation.
Precipitation rate	prec	mm/hr	3-hourly mean (from -3.0 hr to 0.0 hr) precipitation rate.

4.1.3. Albedo

The surface albedo is the ratio of the surface reflected flux of the incoming solar radiation to incoming solar radiation. Albedo is an important parameter in the research of surface energy balance because of the value of albedo determines how much radiation is absorbed by the underlying surface, it is also one of ground surface parameters which have a significant impact on the biosphere and climate processes. Albedo is related to the character of surface, the solar zenith angle and solar spectrum. The traditional method of albedo estimation is to use measured data combined with vegetation characteristics and soil types (Angstrom, 1925; Betts & Ball, 1997; Idso & Jackson, 1975; Wiscombe & Warren, 1980).

For this research, broadband shortwave surface albedo was derived from MODIS Albedo products MCD43B3 considering the needs of the study. This product provides 1 km data with directional hemispherical reflectance (black-sky albedo) at local solar noon and hemispherical reflectance (white-sky albedo). These MCD43B3 albedo quantities are produced from the 16-day models provided in MCD43B1.

4.1.4. Land cover

At present, several researches have increasingly turned to remote sensing data to describe the geographic distribution of land cover at regional scale. Therefore, every year in the China information about types of vegetation can be collected from remote sensing data. For this thesis, the MODIS Land Cover Product (MCD12Q1) was selected due to its up-to-date attribute. It can be downloaded free from NASA Earth Observing System Data and Information System (https://lpdaac.usgs.gov/dataset_discovery/modis/modis_products_table/mcd12q1).

The land cover product derives from MODIS combined Terra and Aqua data after image processing. The MCD12Q1 product provides the dominant land cover type with 0.05° spatial resolution for global area. It applied International Geosphere Biosphere Programme (IGBP) classification approach by supervised classification. The primary land cover scheme of this data identifies 17 land cover classes, which includes 11 natural vegetation classes, 3 developed and mosaicked land classes, and 3 non-vegetated land classes (Table 4-3).

Table 4-3 IGBP land cover classification scheme of MCD12

Code	Land cover	Code	Land cover
0	Water	9	Savannas
1	Evergreen Needleleaf forest	10	Grasslands
2	Evergreen Broadleaf forest	11	Permanent wetlands
3	Deciduous Needleleaf forest	12	Croplands
4	Deciduous Broadleaf forest	13	Urban and built-up
5	Mixed forest	14	Cropland/Natural vegetation mosaic
6	Closed shrublands	15	Snow and ice
7	Open shrublands	16	Barren or sparsely vegetated
8	Woody savannas		

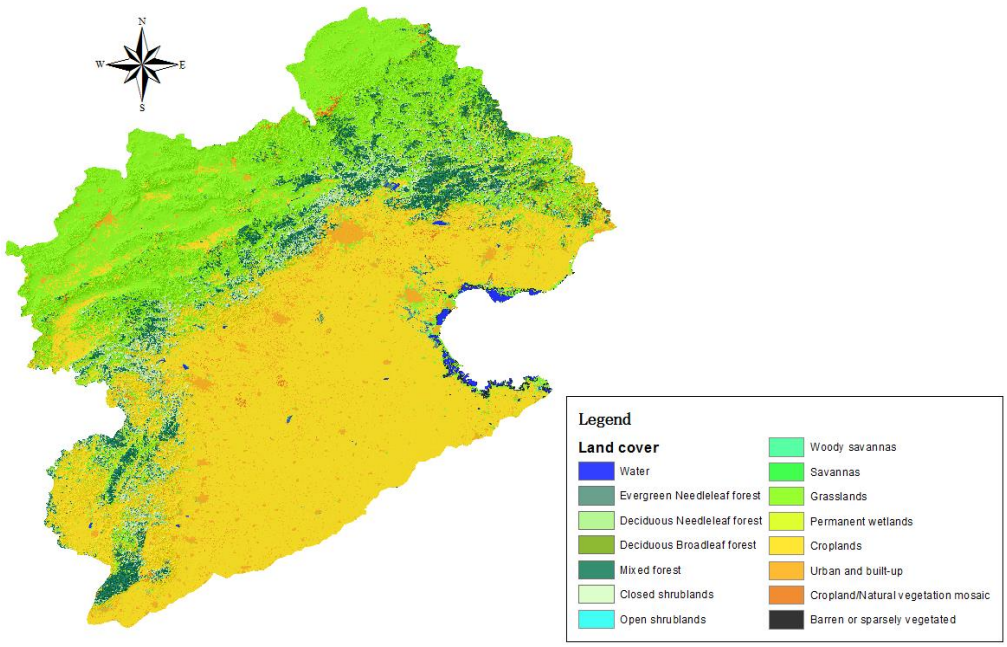

Figure 4-2 Land cover map of Haihe River Basin

4.1.5. NDVI and vegetation fraction

Vegetation index is a simple and effective evaluation of surface vegetation activity, it can reflect evolutionary information of vegetation to some extent. The concept of normalized difference vegetation index (NDVI) was proposed by Deering in 1978, can be combined by Satellite detection data in different bands.

$$NDVI = \frac{NIR - R}{NIR + R} \tag{4-1}$$

where NIR is reflectance in near-infrared band, R is reflectance in red band.
For the ground object, the minimum value of NDVI is near to 0, and the maximum value is about 0.8. A negative value indicates that the ground is covered by clouds, water, and snow which highly reflective to visible light.

Considering the needs of the research, China NDVI synthetic product (MODND1T) in ten days (on days 1, 11 and 21 of each month) are used to this study. This product is processed by MODIS satellite MOD09GA data with splicing, clipping, projection conversion, unit conversion and other processes. The spatial resolution of this data set is 500m, high temporal resolution and high quality (without the influence of the cloud) can used to hourly and daily evapotranspiration estimation.

Vegetation fraction (f_c) corresponds to the fraction of ground surface covered by green vegetation canopy. For SEBS model, f_c can used to evaluate the contributions of vegetation and bare soil to the roughness parameterization. This parameter is sensitive to the vegetation amount, can be derived from NDVI using following equation:

$$f_c = \frac{NDVI - NDVI_{\min}}{NDVI_{\max} - NDVI_{\min}} \tag{4-2}$$

where $NDVI_{max}$ and $NDVI_{min}$ represents the NDVI value for full vegetation and for bare soil in study area respectively.

4.1.6. Land surface emissivity

Land surface emissivity is the ratio of the radiation from the surface to the radiation from an ideal black surface at the same temperature, this parameter is related to the surface composition, surface roughness and wavelength. In the energy balance equation, this physical parameter can used to calculation of net radiation (total longwave radiation emission from the surface). There are several methods to estimate the land surface emissivity. For my study, the relationship will be built between the land surface emissivity and the NDVI value according to the method of Sobrino et al. (2004) and Chen et al. (2013).

4.2. Validation of data

As mentioned in Section 4.1, a variety of remote sensor data and meteorological forcing data are used to estimate the energy flux in this research. These data need to be validated by comparing them with independent data set. According some research (X. Chen et al., 2014; X. Chen, Su, Ma, Yang, & Wang, 2013; Z. Wan, Zhang, & Li, 2004; Yao et al., 2013; Zhang, Kimball, Nemani, & Running, 2010), the energy balance measurement system (four components of radiation, eddy covariance system, automatic meteorological station) is applied for validating the satellite image data, forcing data and the final evapotranspiration product. The validation of satellite data and meteorological forcing data will be made by compared these data sets with five flux stations (Daxing, Miyun, Guantao, Huailai, Luancheng) in Haihe River Basin as indicated before. The validation of these input data can help and analyse reducing ET errors due to input data.

4.2.1. Validation of LST (Land surface temperature)

The land surface temperature in each site is calculated using Stefan-Boltzmann equation, it describes the radiation from a target (black body) in terms of its temperature. This equation written as:

$$R_l^{\uparrow} = \varepsilon \sigma T^4 \tag{4-3}$$

$$T = \left(R_l^{\uparrow} / \varepsilon \sigma \right)^{\frac{1}{4}} \tag{4-4}$$

where T is land surface temperature (LST), $R_l^{\uparrow}$ is upward longwave radiation, ε is the "broad-band" land surface emissivity - assume it is equal to 0.975 in this study; σ is the Stefan–Boltzmann constant (5.67×10^{-8}).

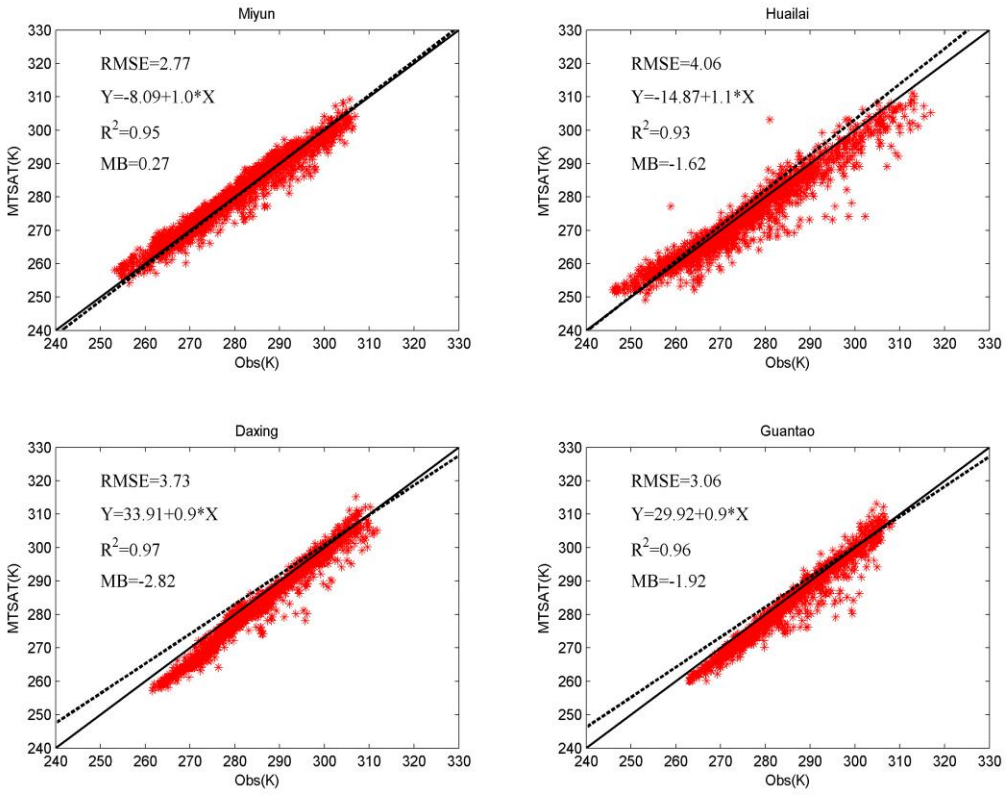

Figure 4-3 The scatter point for LST from MTSAT against in situ measurement

The upward longwave radiation $R_l^{\uparrow}$ in this method can be derived from in situ measurement. The comparisons of LST in four sites are show in Figure 4-3. In this figure, the root mean square error (RMSE), the coefficient of determination (R^2) as well as the mean bias (MB) are used to do the statistical analysis of accuracy. The statistical indicators RMSE and MB are defined as:

$$RMSE = \sqrt{\frac{\sum_{i=1}^{N}(X_i - X_{o,i})^2}{N}} \tag{4-5}$$

$$MB = \frac{\sum_{i=1}^{N}(X_i - X_{o,i})}{N} \tag{4-6}$$

where X_i is the satellite value or modelled variable value, $X_{o,i}$ is observed value and N is the sample number.

4.2.2. Validation of radiation from ITPCAS

In order to analyse the calculation errors, the downward radiation from China Meteorological Forcing Dataset (ITPCAS) were all validated against station observation (Daxing, Miyun, Guantao, Huailai). The Figure 4-4 shows that a well-fitting between two data source. Besides, compared this validation result with other reference (X. Chen et al., 2014), indicated the R^2 of SWD validation in this study is larger than the reference and the R^2 of LWD is smaller than the reference (Table 4-4); The MB value in this validation is less than the reference.

Table 4-4 Comparison of the accuracy of radiation from ITPCAS against in-situ measurement

	This study		Reference	
	SWD	LWD	SWD	LWD
Slope	0.9	1.0	0.95	0.91
Intercept	13.27	7.67	13.6	-0.66
RMSE	73.81	22.08	28.3	32.8
R^2	0.91	0.925	0.89	0.98
MB	-1.29	-0.01	-5.7	28.9

Downward shortwave radiation

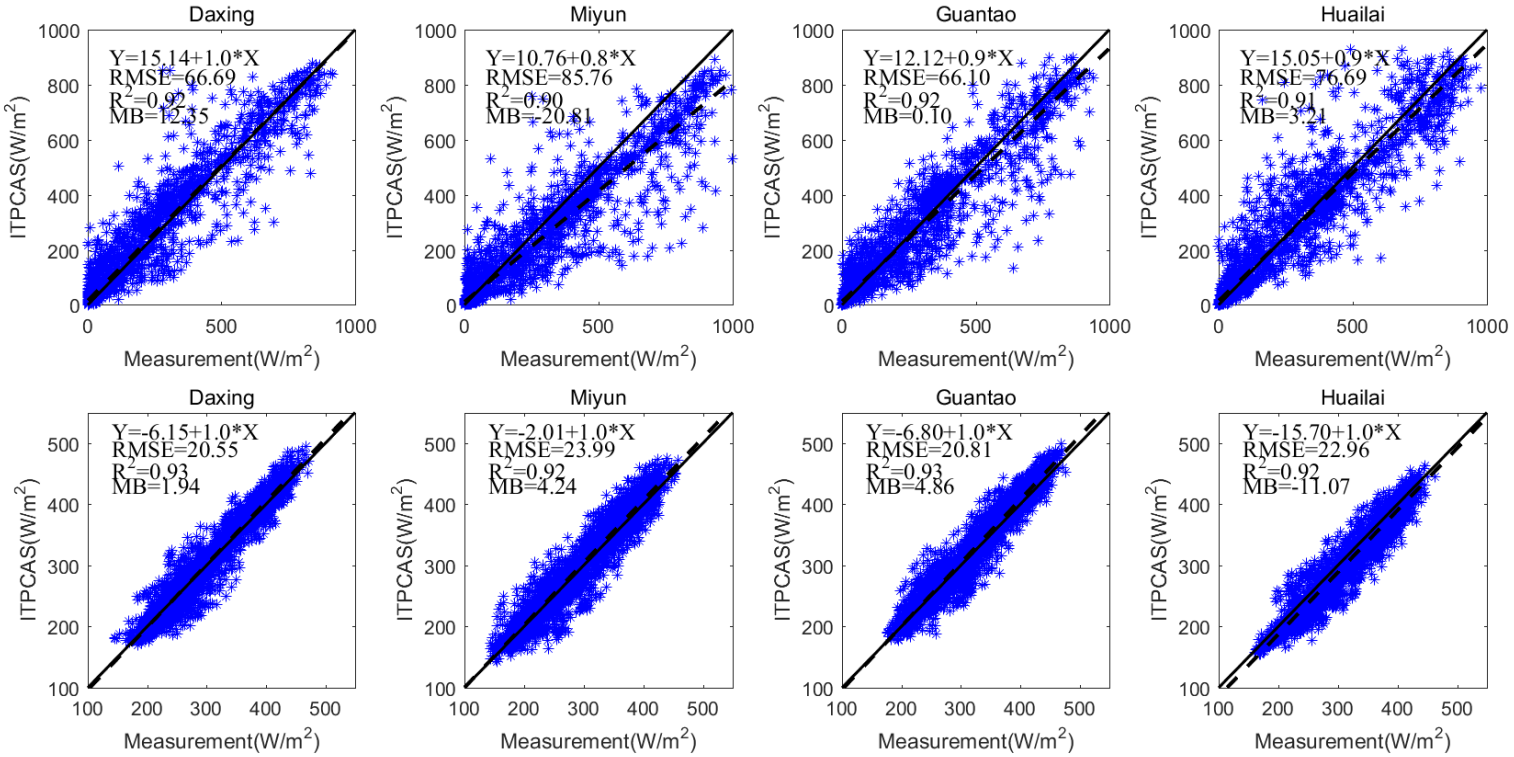

Downward longwave radiation

Figure 4-4 The scatter point for downward shortwave radiation and longwave radiation from ITPCAS against in situ measurement

5. SURFACE ENERGY BALANCE SYSTEM (SEBS)

A Surface Energy Balance System (SEBS) was developed by Su (2002). The model is proposed for the estimation of turbulent heat fluxes and evaporative fraction by using satellite earth observation data, in combination with meteorological information at regional scales. SEBS has been widely applied for ET and land surface flux estimation(L. Jia et al., 2003; R. Liu, Wen, Wang, & Zhang, 2015; Rwasoka et al., 2011; Zhan, Zhao, Wang, & Yin, 2011). This study used the modified model version in Chen et al (2013), which has revised the roughness length for heat transfer, and makes the model more suitable in the application of the regional scale.

SEBS model requires land cover structural parameters (leaf area index, vegetation height), remote sensing products (land surface temperature, albedo, emissivity, down-welling surface shortwave and longwave radiation, fraction of vegetation cover, NDVI, and DEM), and metrological data such as air pressure, temperature, specific humidity, wind speed (Su, 1996; Su, Pelgrum, & Menenti, 1999).

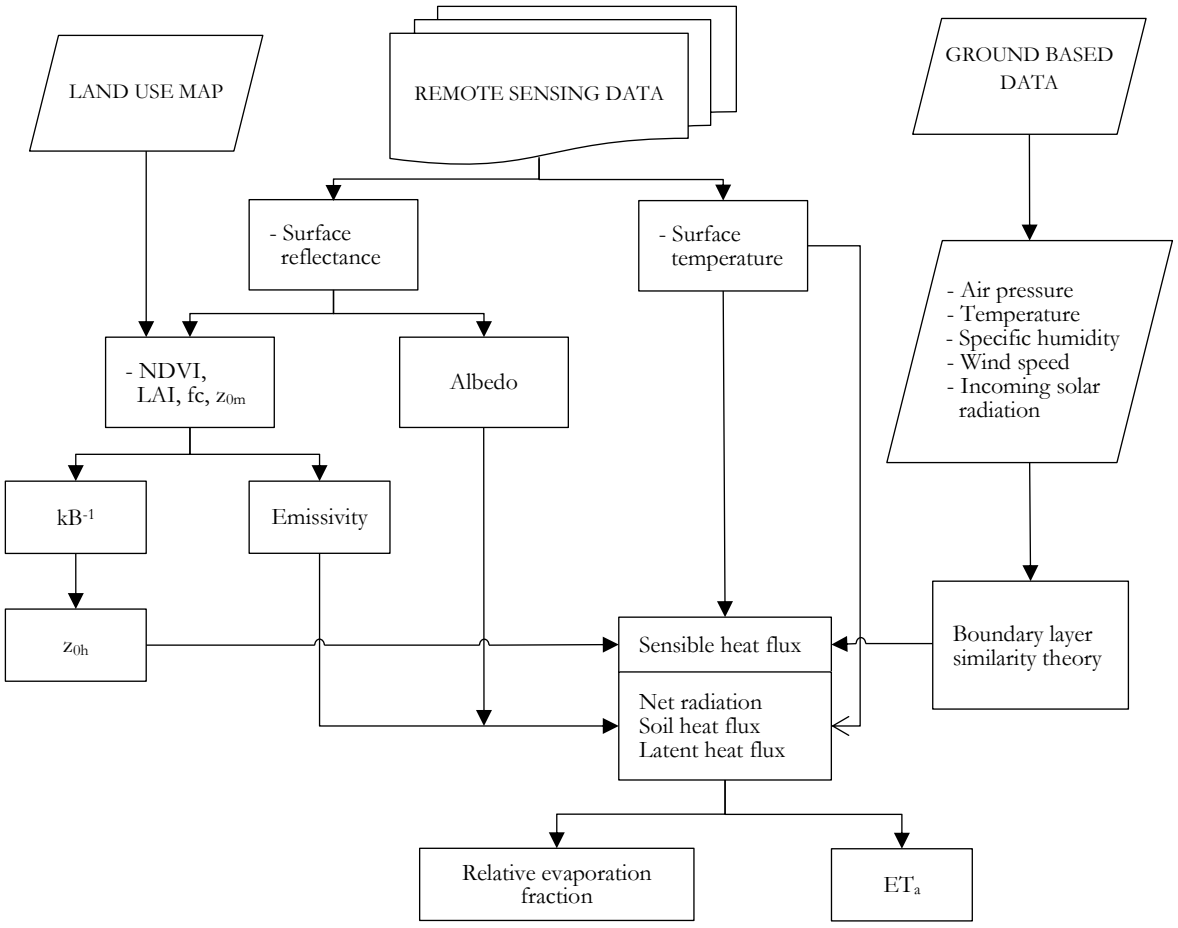

Figure 5-1 Flowchart of SEBS model

5.1. The theory of SEBS model

The electromagnetic radiation which emitted by sun, only 51% of radiation can reach the surface in the form of direct light and scattering. And 30% of them reflected back to space by the Earth's surface or louds and atmospheric particles. The remaining 19% of total radiation is absorbed by the atmospheric gases, particles, and clouds (Pidwirny, 2006). The part of energy that reaches the surface is converted to other forms, such as heat the Earth's surface and lower atmosphere, melt and evaporate water, keeps the energy in balance. This process of energy flux exchange can be expressed as a surface energy balance equation, it is the principle of SEBS model:

$$R_n = G_0 + H + \lambda E \tag{5-1}$$

where R_n is the solar net radiation; G_0 is the soil heat flux; H is the turbulent sensible heat flux from the underlying surface to the atmosphere; λE is the turbulent latent heat flux from the underlying surface to the atmosphere, λ is the latent heat of vaporization, E is actual evapotranspirationion (Su, 2002).

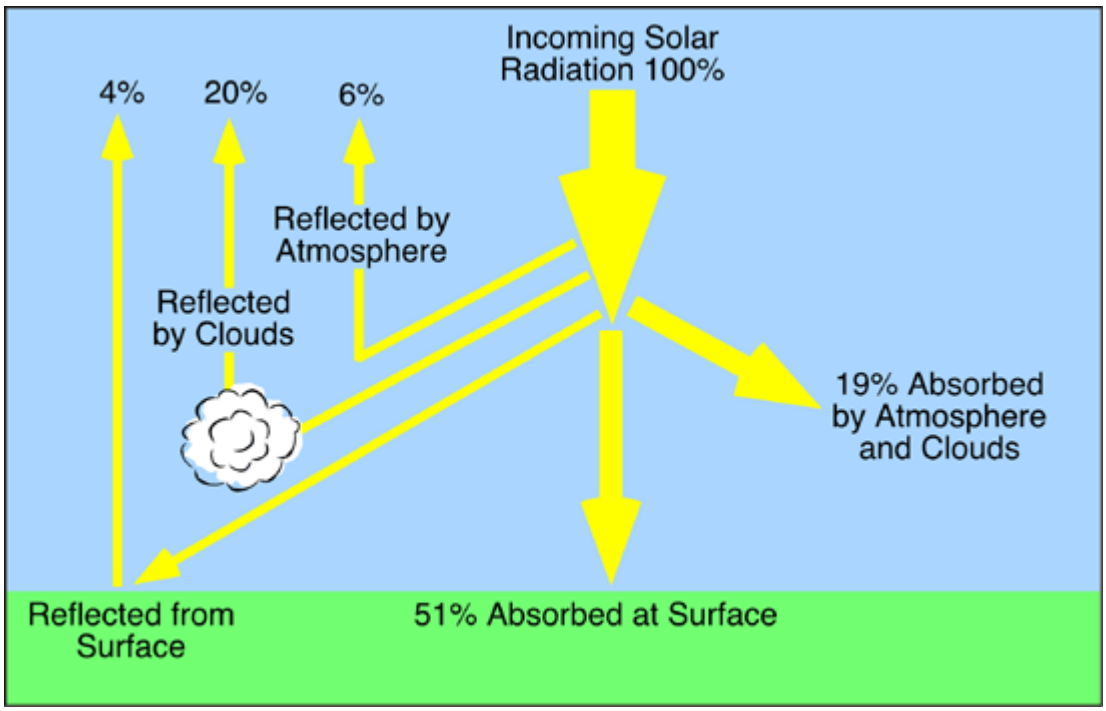

Figure 5-2 The atmospheric and surface processes of solar radiation (Pidwirny, 2006)

5.2. Net radiation

Surface net radiation is also called radiation balance or radiation budget (Planton, 2013). The net radiation is the driving force of ground energy, material transport and exchange process, thus the variation of net radiation will result in variation in other components of the surface heat balance. The net radiation is the difference value between the income and outcome of surface shortwave and longwave radiation, and the surface radiation balance equation which can calculate the net radiation is expressed as:

$$R_n = R_{ns} + R_{nl} \tag{5-2}$$

$$R_n = R_s^{\downarrow} - R_s^{\uparrow} + R_l^{\downarrow} - R_l^{\uparrow} \tag{5-3}$$

$$= (1-\alpha)R_s^{\downarrow} + R_l^{\downarrow} - \varepsilon_s \sigma T_s^4 \tag{5-4}$$

where R_n is the solar net radiation; $R_s^{\downarrow}$ is downward shortwave radiation, which is total solar radiation; $R_s^{\uparrow}$ is reflected shortwave radiation; $R_l^{\downarrow}$ and $R_l^{\uparrow}$ is downward and upward longwave radiation respectively; α is surface albedo; ε_a is emissivity of atmosphere and ε_s is land surface emissivity; σ is Stefan-Boltzmann constant, equal to 5.67×10^{-8} ; T_a and T_s is air temperature and land-surface temperature respectively. α , ε_s and T_s can be derived from remote sensing data in visible and thermal inferred channel. $R_l^{\downarrow}$ and T_a are obtained from meteorological observation data.

5.3. Soil heat flux

After the surface of soil absorbs solar radiation, heat flux will transfer to the lower soil layer. On the contrary, heat will be transferred from the soil when the soil temperature lower than the deep layer soil temperature. This process is the soil heat exchange process.

Soil heat flux is an important component which has an effect on soil evaporation and surface energy exchange. It refers to heat exchange within the soil, determined as an unfixed percentage of energy:

$$G_0 = R_n \cdot \left[\Gamma_c + (1-f_c)\cdot(\Gamma_s - \Gamma_c)\right] \tag{5-5}$$

where, Γ_c , Γ_s is empirical coefficient under full vegetation canopy and bare soil; An interpolation is performed between these limiting cases using the fractional canopy coverage, f_c , can be calculated from NDVI. G0 calculation for water, snow, and urban area can be referred to Chen et al.(2013).

5.4. Sensible heat flux

Sensible heat flux is the energy transfer to the atmosphere by turbulent due to the effect of temperature difference, that is a part of energy which used to heat the air.

5.4.1. Zero plane displacement height, roughness height for momentum transfer and heat transfer

To calculate sensible heat flux accurately, the zero-plane displacement height and dynamic roughness parameters need to be determined. Roughness height for heat transfer is hard to estimate because of the influence of terrain, environmental variables and the underlying surface conditions. Due to this reason, the estimation of surface turbulent flux and evaporation fraction has large uncertainty by means of the surface radiation temperature. The zero plane displacement height d_0, roughness height for momentum transfer z_{0m} and roughness height for heat transfer z_{0h} can be derived from the following equations derived by Massman (1999) and discussed in Su et al. (2001) and Chen et al.(2013). In this method, the zero-plane displacement height d_0 is modelled as:

$$d_0 / h = 1 - \frac{1}{2n_{ec}}\left[1 - \exp(-2n_{ec})\right] \tag{5-6}$$

which h is the height of canopy (m), n_{ec} is the wind speed profile extinction coefficient in the canopy can be calculated using Equation (5-7):

$$n_{ec} = \frac{C_d \cdot LAI}{2u_*^{\,2} / u(h)^2} \tag{5-7}$$

where $u(h)$ is the horizontal wind speed at the canopy height, C_d is the drag coefficient of the foliage elements. *LAI* is the one-side leaf area speed at the canopy top, can derived from NDVI. And u_* is the friction velocity, the ratio $u_* / u(h)$ is:

$$u_* / u(h) = C_1 - C_2 \exp(-C_3 C_d \times LAI) \tag{5-8}$$

where C_1 (= 0.38), $C_2 (= C_1 + k / \log(0.0025))$ and C_3 (=15.1) are model constants related to the bulk surface drag coefficient (W. J. Massman, 1997; William J Massman, Forthofer, & Finney, 2017), k is the von Karman constant in here equal to 0.4. Then, the roughness height for momentum transfer and the roughness height for heat transfer can be calculated by equations:

$$z_{0m} = h\left[1 - (d_0 / h)\right]\exp(-k \cdot u(h) / u_*) \tag{5-9}$$

$$z_{0h} = z_{0m} / \exp(kB^{-1}) \tag{5-10}$$

where z_{0m} is the roughness height for momentum transfer and z_{0h} is the scalar roughness height for heat transfer. B^{-1} is the inverse Stanton number, a dimensionless heat transfer coefficient.

For the equation above, kB^{-1} is treated as a fixed value or z_{0h} is the empirical value in the general study of the energy balance model. However, the SEBS model developed the parameterized method Equation (5-11) of kB^{-1} and reduced the error of the scalar roughness height for heat transfer uncertainty (Su et al., 2001). This point is the main innovation of the SEBS model.

$$kB^{-1} = f_c^{\,2} kB_c^{-1} + 2 f_c f_s kB_m^{-1} + f_s^{\,2} kB_s^{-1} \tag{5-11}$$

where f_c is the fractional canopy coverage and f_s is that of soil; kB_c^{-1} is the kB^{-1} for the canopy, kB_s^{-1} is the kB^{-1} for bare soil and kB_m^{-1} is the kB^{-1} for mixed the canopy and bare soil. kB_c^{-1} and kB_m^{-1} can be derived from Equation (5-12) purposed by Choudhury and Monteith (1988).

$$kB_c^{-1} = \frac{k \cdot C_d}{4 \cdot C_t \cdot \frac{u_*}{u(h)}(1 - e^{-n_{ec}/2})} \tag{5-12}$$

$$kB_m^{-1} = \frac{k \cdot \frac{u_*}{u(h)} \cdot \frac{z_{0m}}{h}}{C_t^*} \tag{5-13}$$

where C_t is heat transfer coefficient of the leaf, C_t^* is heat transfer coefficient of soil.

For kB_s^{-1}, most research used the method of Brutsaert (1982). Chen et al.(2013) updated the calculation of kB_s^{-1} using a better method of roughness heat parameterization (K Yang, Koike, Fujii, Tamagawa, & Hirose, 2002). In this study, the method developed by Chen et al (2013) will be introduced to calculate kB_s^{-1} which has been assessed for the ability of improving the accuracy of sensible heat flux estimation. It is given as follows:

$$z_{0h} = (70\vartheta / u_*)\exp(-7.2u_*^{0.5}\theta_*^{0.25}) \tag{5-14}$$

$$kB_s^{-1} = \log(\frac{z_{0m}}{z_{0h}}) \tag{5-15}$$

where ϑ is the kinematic viscosity of air ($1.5*10^{-5}$ m^2/s), θ_* is the surface friction temperature.

5.4.2. The calculation of sensible heat flux

The theory of boundary layer has the similarity relationships for the profiles of the mean speed and the mean temperature (θ_0-θ_a), this relationship can be expressed as Equations (5-16) and (5-18) . The friction velocity, sensible heat flux and Obukhov length can be obtained by solving the following equations:

$$u = \frac{u_*}{k}\left[\ln\left(\frac{z-d_0}{z_{0m}}\right) - \psi_m\left(\frac{z-d_0}{L}\right) + \psi_m\left(\frac{z_{0m}}{L}\right)\right] \tag{5-16}$$

$$\theta_0 - \theta_a = \frac{H}{ku_*\rho C_p}\left[\ln\left(\frac{z-d_0}{z_{0h}}\right) - \psi_h\left(\frac{z-d_0}{L}\right) + \psi_h\left(\frac{z_{0h}}{L}\right)\right] \tag{5-17}$$

$$L = \frac{\rho \cdot C_p \cdot u_*^3 \cdot \theta_v}{k \cdot g \cdot H} \tag{5-18}$$

where u is mean speed in the reference height z , z is the height above the surface. u_* is the friction velocity, k is von Karman's constant (equal to 0.4). ψ_m and ψ_h are the stability correction functions for momentum transfer and sensible heat transfer respectively. θ_0 is the potential temperature at the surface, θ_a the potential temperature at height z . ρ is density of air, C_p is specific heat capacity of air. H is the sensible heat flux. L is Obukhov length, g is the acceleration due to gravity and θ_v is the potential virtual temperature near the surface.

The express form of the stability correction function for momentum transfer and sensible heat transfer depending on the reference height.

5.5. Determination of evaporation fraction

In order to determine the evaporation fraction, we need to consider the energy balance relationship in the limit condition. When the ground is extreme dry, the sensible heat flux will reaches its maximum value because of the latent heat flux (or evaporation) is zero due to the limitation of soil moisture. According Equation (5-1), it can be expressed as:

$$\lambda E_{dry} = R_n - G_0 - H_{dry} \equiv 0 \tag{5-19}$$

o $$H_{dry} = R_n - G_0 \tag{5-20}$$

Under the wet-limit, the sensible heat flux will be reached its minimum value, it can be expressed as:

$$\lambda E_{wet} = R_n - G_0 - H_{wet} \tag{5-21}$$

or $$H_{wet} = R_n - G_0 - \lambda E_{wet} \tag{5-22}$$

Relative evaporation is given by:

$$\Lambda_r = \frac{\lambda E}{\lambda E_{wet}} = 1 - \frac{\lambda E_{wet} - \lambda E}{\lambda E_{wet}} \tag{5-23}$$

$$\Lambda_r = 1 - \frac{H - H_{wet}}{H_{dry} - H_{wet}} \tag{5-24}$$

Finally, the evaporation fraction can be calculated by:

$$\Lambda = \frac{\lambda E}{R_n - G} = \frac{\Lambda_r \cdot \lambda E_{wet}}{R_n - G} \tag{5-25}$$

5.6. Actual evapotranspiration

According Equation (5-25), the actual sensible heat flux and the latent heat flux can be calculated. 3-hourly and daily net radiation is given by:

$$R_{n3} = (1-\alpha) K_3^{\downarrow} + L_3 \tag{5-26}$$

$$R_{n24} = (1-\alpha) K_{24}^{\downarrow} + L_{24} \tag{5-27}$$

where K is total incident radiation, L is long-wave radiation.

3-hourly ET and daily ET is:

$$ET_{3h} = 1.08 \times 10^7 \times \Lambda \times \frac{R_{n3}}{\lambda \rho_w} \tag{5-28}$$

$$ET_{daily} = 8.63 \times 10^7 \times \Lambda \times \frac{R_{n24}}{\lambda \rho_w} \tag{5-29}$$

where ET_{3h} is the 3-hours actual evapotranspiration (mm/3h), ET_{daily} is daily actual evapotranspiration (mm/d). ρ_w is density of water, λ is latent heat of vaporization as follows:

$$\lambda = (2.501 - 0.002361 \times T) \quad \text{MJ/kg} \tag{5-30}$$

6. RESULTS AND DISCUSSION

This topic based on the SEBS model estimates the net radiation, ground heat flux using satellite image and meteorological data, then the sensible heat flux can be obtained. After that, we got the instantaneous latent heat flux and instantaneous evapotranspiration by energy residual methods. Finally, time scale extension was used to calculate hourly and daily evapotranspiration according instantaneous evapotranspiration. In addition to this, 4 tests developed by Chen et al. (2013) were used to choose the best roughness length parameterization method in order to obtain better ET results. Finally, the method of test No.3 were applied to this research. More details about the four roughness length parameterization methods could be discussed with Dr. Xuelong Chen directly through email x.chen@utwente.nl.

6.1. The surface characteristic parameter analysis

6.1.1. Land surface temperature

Land surface temperature is a significant parameter for energy balance system. As we can see from the Figure 6-1 and Figure 6-2, land surface temperature in September 2010 range from 285 to 310K, and the land surface temperature difference of a day is about 15K in study area. For the four measurement stations (Daxing, Miyun, Guantao and Huailai) during this period, the land surface temperature at Daxing is higher than other stations, the next is Guantao, and Miyun station; The lowest temperature was observed at Miyun station which located in north of study area.

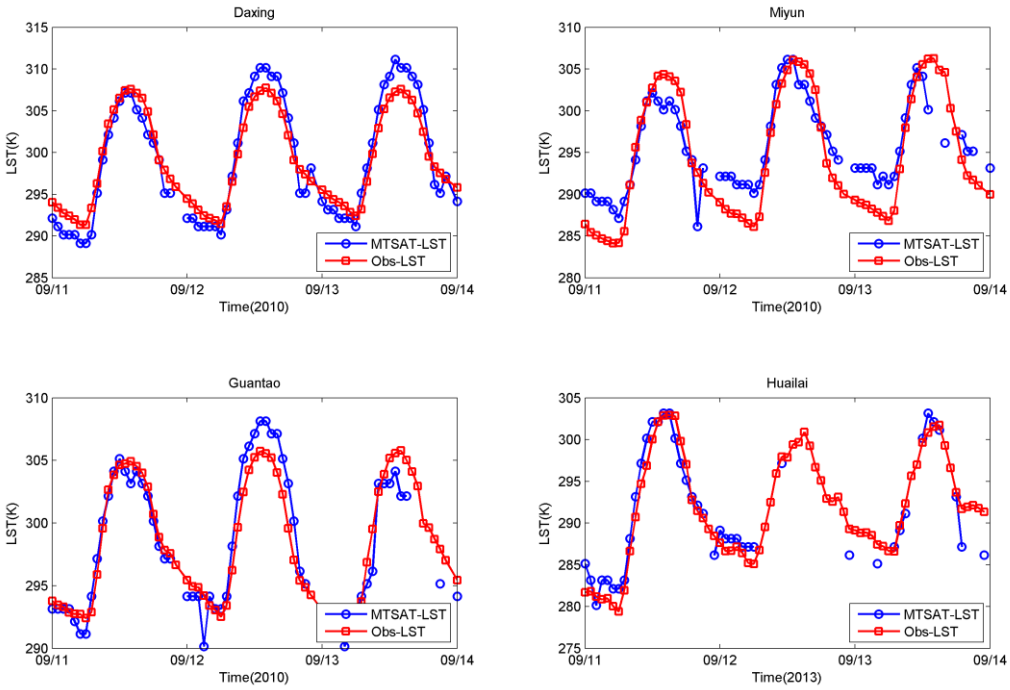

Figure 6-1 Time series of LST derived from MTSAT and measurements at four stations (Daxing, Miyun, Guantao and Huailai)

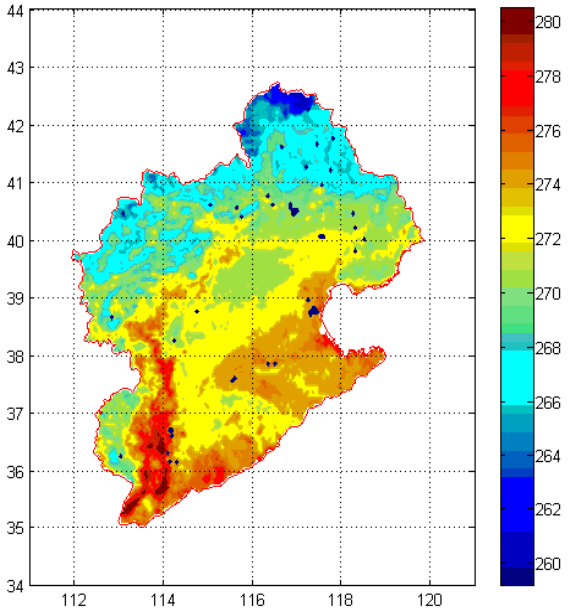

Figure 6-2 Land surface temperature map at 14:00 10 Dec 2010 for Haihe River Basin (K)

It can be seen from the figure above, the land surface temperature gradually increased from north to south in Haihe River Basin, low temperature mainly concentrated in the area with more vegetation and high altitude. The temperature difference between north and south of study area is about 18K.

6.1.2. NDVI

As indicated in section 4.1.5, NDVI can reflect evolutionary information of vegetation to some extent, detect vegetation growth status, vegetation coverage and eliminate partial radiation errors. Figure 6-3 is time series comparison of NDVI derived from MODND1T at five stations, it shows the NDVI annual characteristics of the study area. The high NDVI mainly concentrated in summer (June to September), and low value focus on winter (January to March). The NDVI in Miyun station is higher than other site, mainly because the vegetation type of Miyun is orchard and not like other sites is crop. The NDVI in Guantao and Luancheng station has two peaks, that is because there are two crops for winter and summer.

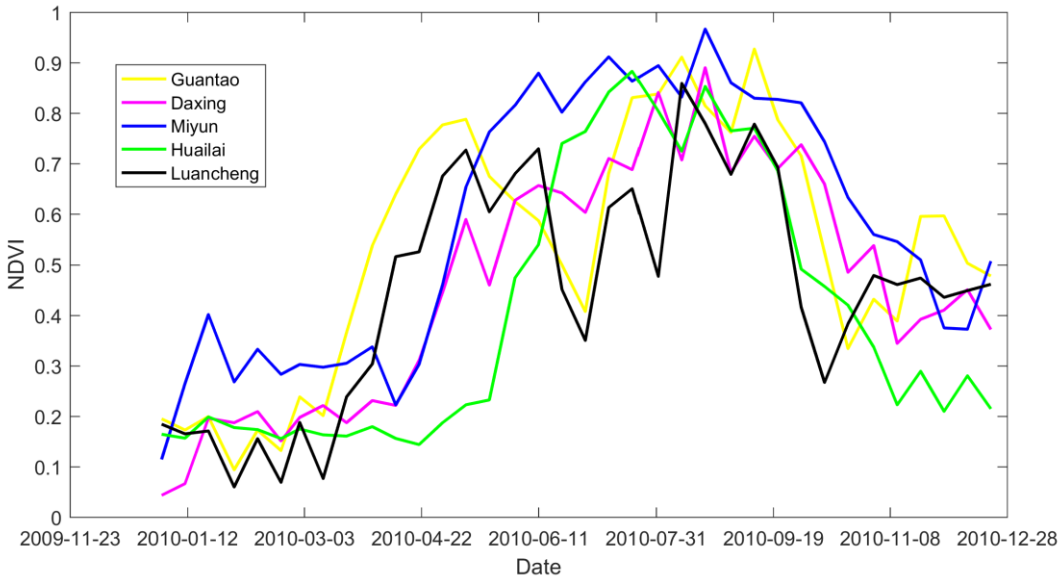

Figure 6-3 Time series of NDVI derived from MODND1T at five stations over Haihe River Basin

6.1.3. Radiation

Shortwave radiation and longwave radiation are important parameters as SEBS model input datasets, they directly determine the amount of radiation reaching the ground surface. Figure 6-4 indicated time series comparison of downward radiation derived from ITPCAS and measurements at five stations. The downward shortwave radiation closely match the in-situ observations relatively, the observed values are slightly larger than the forcing dataset values.

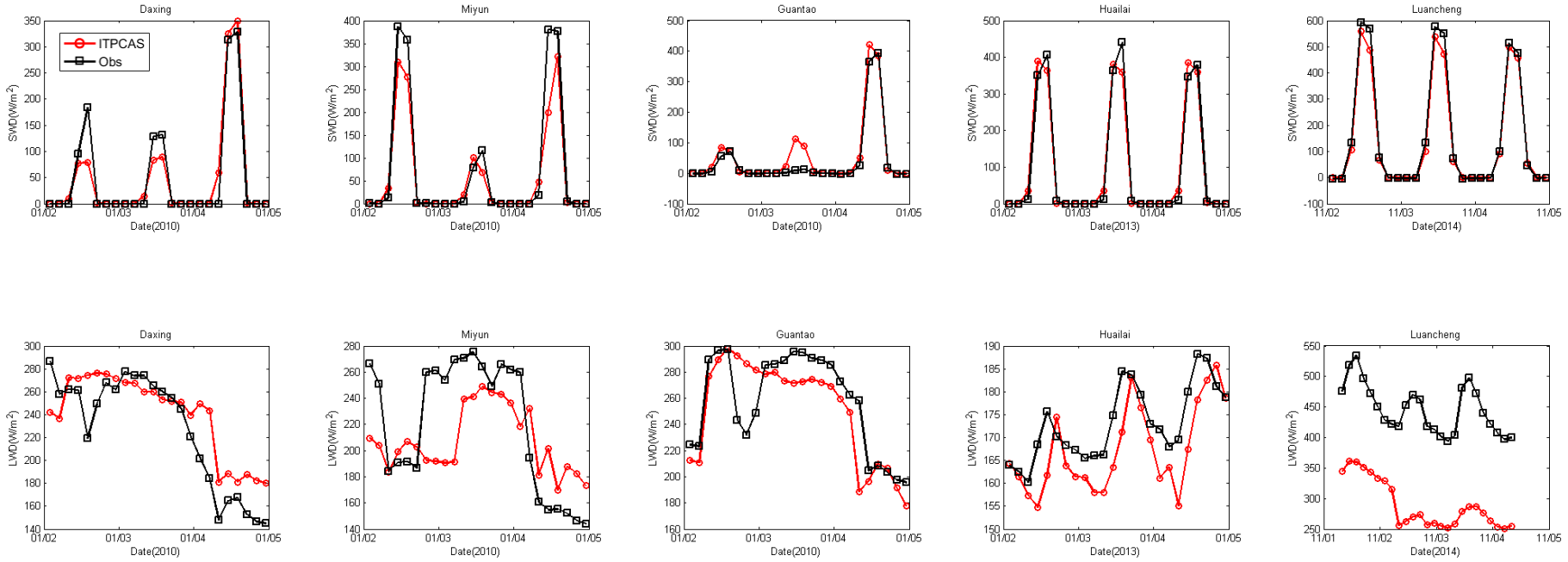

Figure 6-4 Time series of shortwave radiation and longwave radiation derived from ITPCAS and measurements at five stations

6.2. Actual evapotranspiration

6.2.1. Eddy covariance flux tower data

Latent heat flux from the eddy covariance flux tower was used for validating the hourly and daily evapotranspiration derived from the SEBS model as well as in situ measurement. Energy balance closure, requires that the sum of the estimated latent and sensible heat flux be equivalent to all other energy as indicted in Equation (5-1). But most of current studies have shown that the surface energy balance from EC is not balanced.

Energy balance closure is directly relevant to the evaluation of latent and sensible heat fluxes and not to other scalar fluxes (Wilson, 2002). Compared to the energy balance equation, the energy balance closure from eddy covariance is imbalance. Therefore, the energy balance closure of Daxing, Miyun and Guantao site need to be evaluated first. The closure error can be determined by the plotting the sum of the turbulent heat flux against the energy flux (Thomas et al., 2010). The result of energy balance closure of the eddy covariance flux tower is shown in Figure 6-5.

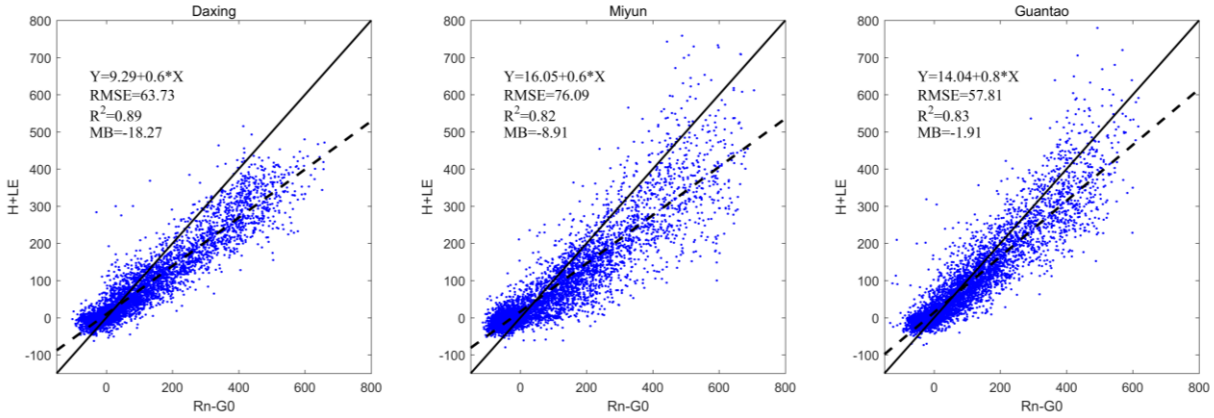

Figure 6-5 Energy balance closure for the flux tower in Daxing, Miyun and Guantao

As shown in the above figure, the slope of the plot indicated an energy balance closure almost ranged from 0.6 to 0.8, the surface energy fluxes (LE + H) are underestimated by about 20–30% relative to estimates of available energy (Rn-G0). The mean coefficient of determination (R^2) in this scatter diagram was 0.85, ranging from 0.82 to 0.89. According to the research of Foken (2008), it belong to the range of 70%~80% it suggested.

Then, the actual evapotranspiration based on in-situ measure at each station was derived from latent heat flux as follows:

$$ET = \frac{\lambda E}{\lambda} \tag{6-1}$$

where λ is latent heat of vaporation, assume it equal to 2440 MJ/kg in here.

6.2.2. Validation of the energy flux results

SEBS 3-hourly and daily maps were obtained by using Equation (5-1)- (5-30). In order to analysis the reliability of the energy flux results, the net radiation, ground heat flux, sensible heat flux, latent heat flux as well as the 3-houly evapotranspiration were all validated against all observation stations based on point measurement. The result of the mean statistical error analysis from all stations are presented in Table 6-1. The time of result range from 2010, 2013 and 2014, removed all null value due to cloud effects from the result in order to reduce the error. The validation of net radiation, ground heat flux, sensible heat flux, latent heat flux was used instantaneous value.

Table 6-1 Statistical results of the error analysis on 3 hourly SEBS estimates from five flux tower

	R_n (W/m²)	G_0 (W/m²)	H (W/m²)	LE (W/m²)	ET(mm/3h)	Mean
Slope	1.0	0.9	0.9	1.1	1.4	1.06
Intercept	-13.25	10.28	0.57	9.48	0.03	1.42
RMSE	50.73	33.83	47.06	57.93	0.32	37.97
R^2	0.94	0.63	0.58	0.65	0.67	0.69
MB	-16.35	10.57	-3.32	11.72	0.08	0.54
Sample	2615	1759	1442	1930	1490	1847

Based on the statistical result, this table shows that net radiation has relatively higher RSME, R^2 and MB. The statistical value of G_0, H, LE is lower than R_n, especially the sensible heat flux. Scatter diagram between SEBS results and eddy covariance results at five stations is shown Figure 6-6 to Figure 6-10.

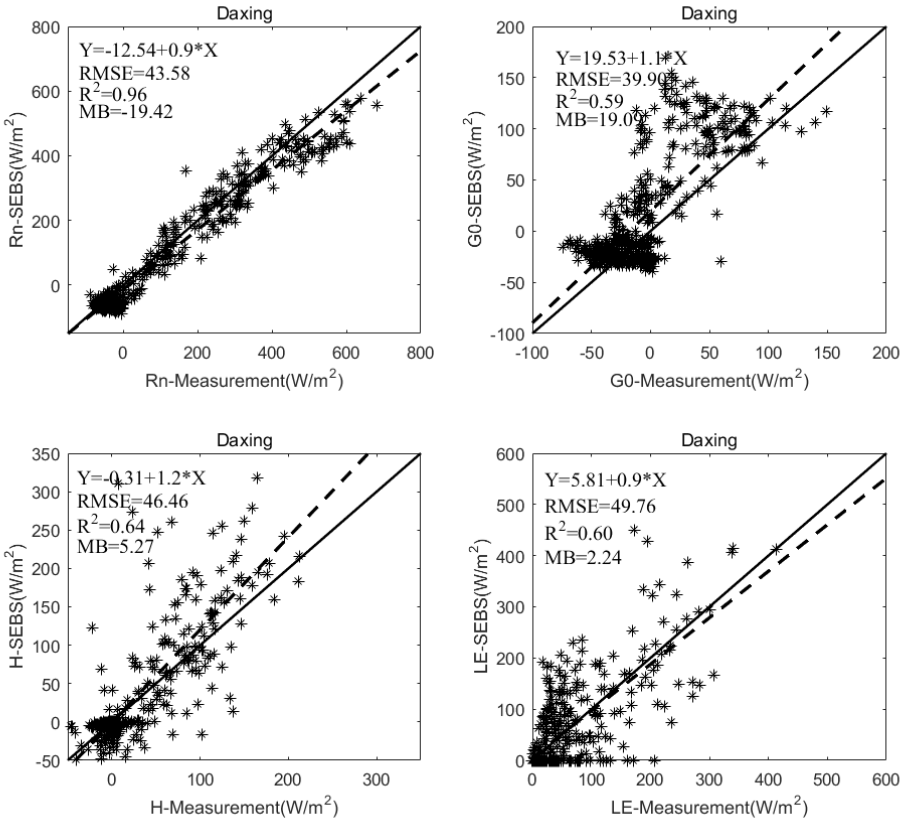

Figure 6-6 Scatter plot between SEBS results and eddy covariance results at Daxing station (2010)

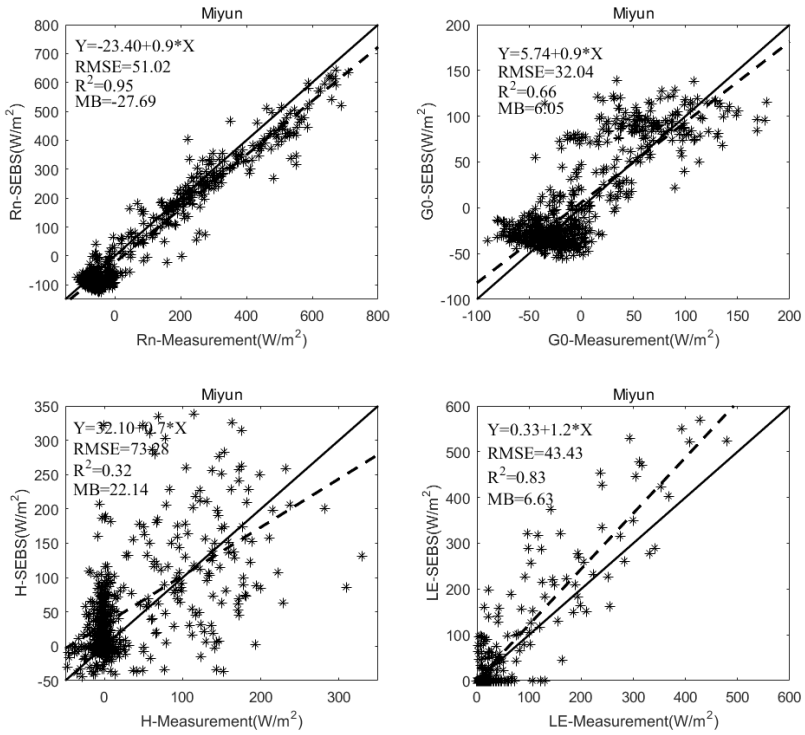

Figure 6-7 Scatter plot between SEBS results and eddy covariance results at Miyun station (2010)

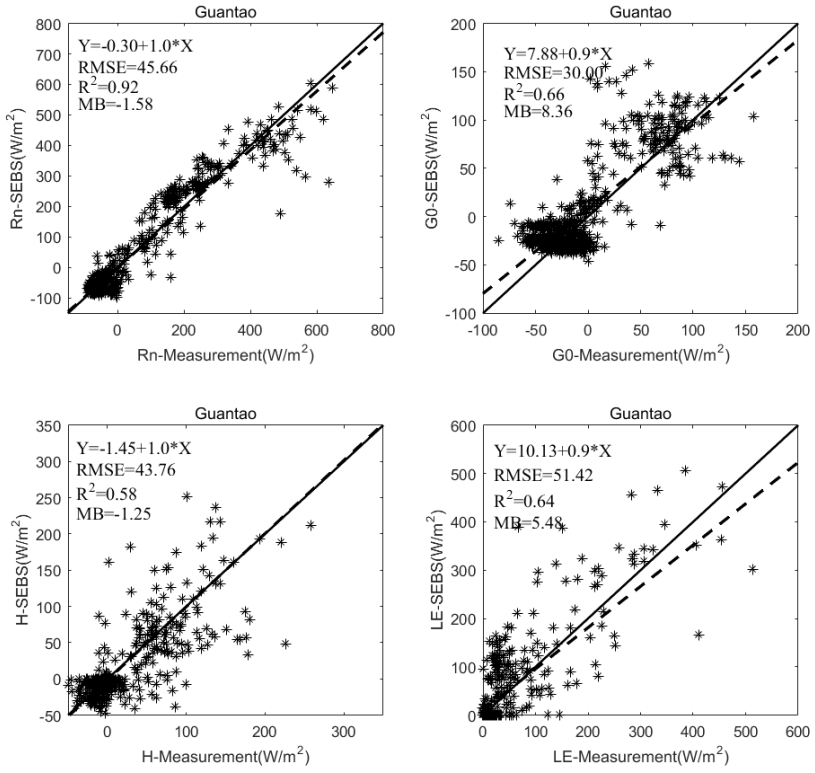

Figure 6-8 Scatter plot between SEBS results and eddy covariance results at Guantao station (2010)

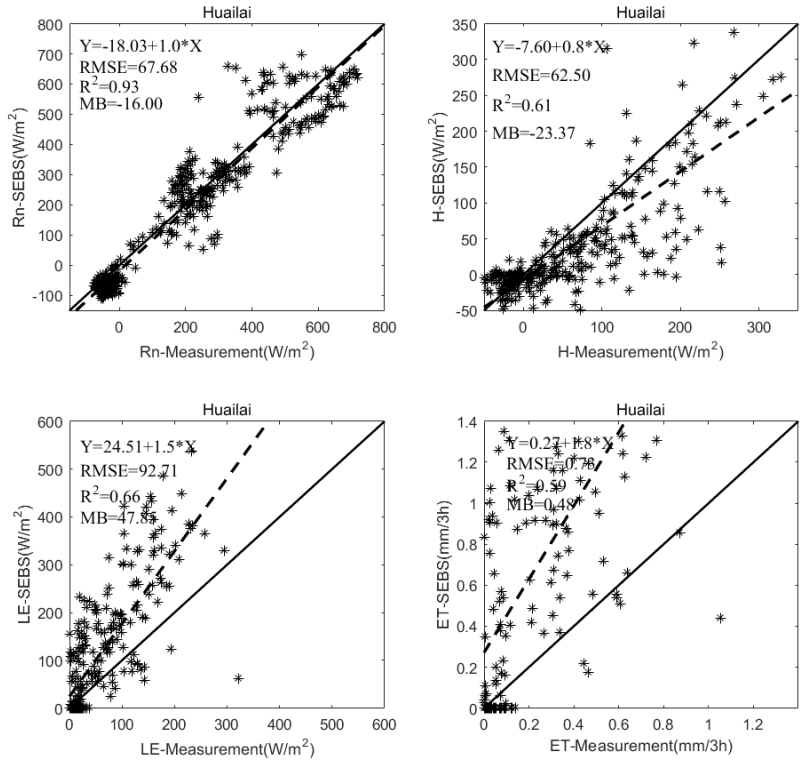

Figure 6-9 Scatter plot between SEBS results and eddy covariance results at Huailai station (2013)

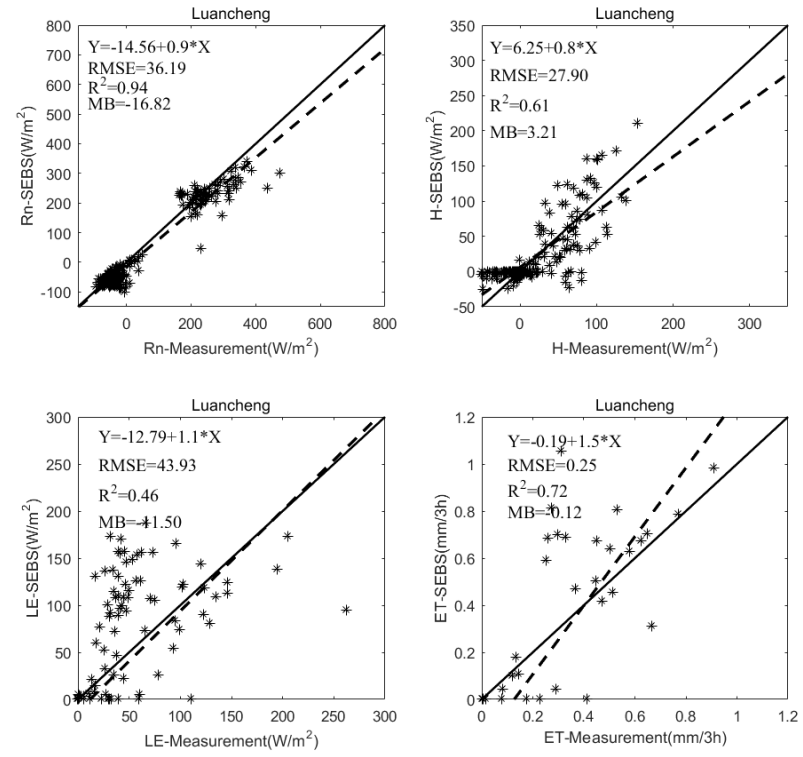

Figure 6-10 Scatter plot between SEBS results and eddy covariance results at Luancheng station (2014.11-12)

From these scatter figures above, the validation result in Daxing station is much better than other stations. All of stations have a good performance for net radiation. For the latent heat flux, the R^2 of validation result reaching 0.83 in Miyun station, and MB is 6.63, this result is good relatively compared to other stations

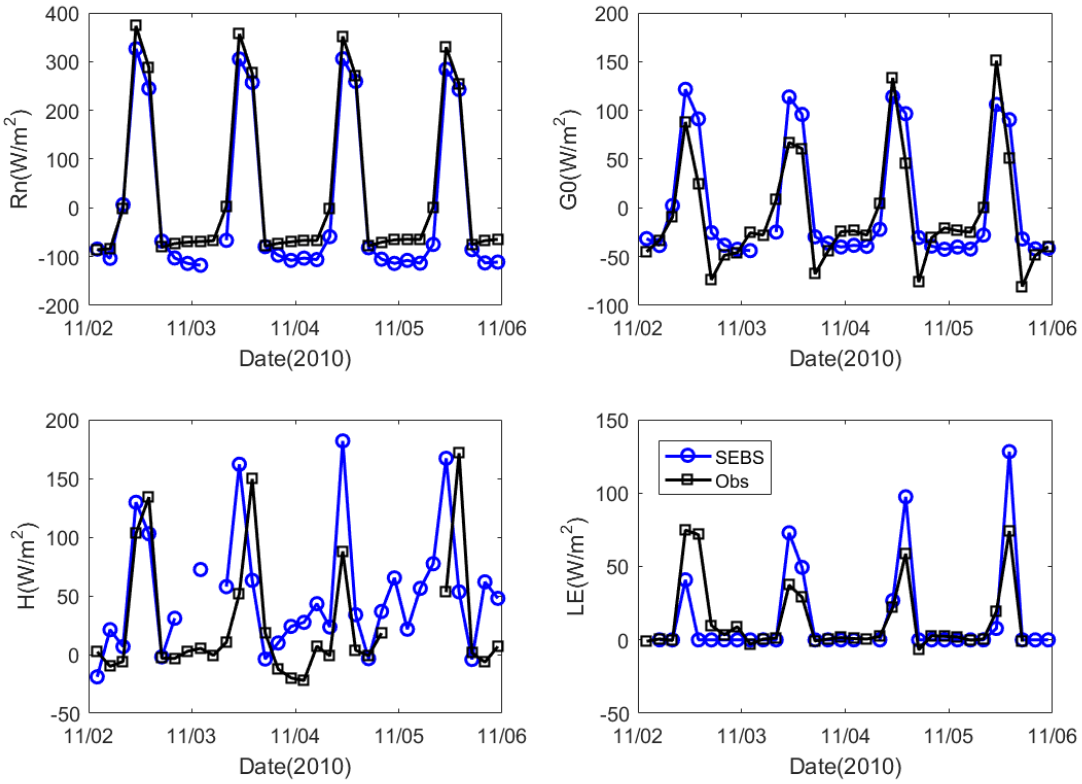

Figure 6-11 Time-series comparison of SEBS output against measurement at Miyun station

Figure 6-11 shows time-series comparison of SEBS output against measurement at Miyun station. It indicated that the trend of energy flux (R_n, G_0, H, LE) from SEBS model is similar as the in-situ observation. The net radiation, is the driving force of ground energy, material transport and exchange process, thus the variation of net radiation will result in variation in other components of the surface heat balance. It is mainly calculated by the incident and reflected total solar shortwave radiation and ground long wave radiation, the value of R_n from SEBS result is lower than the observation because of the atmospheric effects. Oppositely, the value of SEBS sensible heat flux is larger than the measured. The distribution range of sensible heat flux is large, which reflects the complexity of the underlying surface and the uneven distribution of land surface temperature and wind speed. Therefore, it is a challenge to estimate high temporal sensible heat flux in study area due to the topographical conditions and urbanization.

In addition, compared this study validation results with other similar research. Gao et al. (2012) using Thornthwaite water balance method to estimated spatial and temporal characteristics of actual evapotranspiration over the Haihe River basin during 1960–2002, conclusions is consistent with this study comparatively.

6.2.3. Distribution of actual ET

6.2.3.1. Spatial distribution of hourly and daily ET

Several 3-hourly ET maps was obtained using SEBS model, daily ET maps can be calculated by summing eight images of 3-hourly ET. Final hourly and daily ET maps are shown in Figure 6-12 and Figure 6-13. Based on these maps, higher evapotranspiration is observed at 11:00 to 14:00 due to increasing land surface temperature. The variation of evapotranspiration in a day is about 1.5 mm.

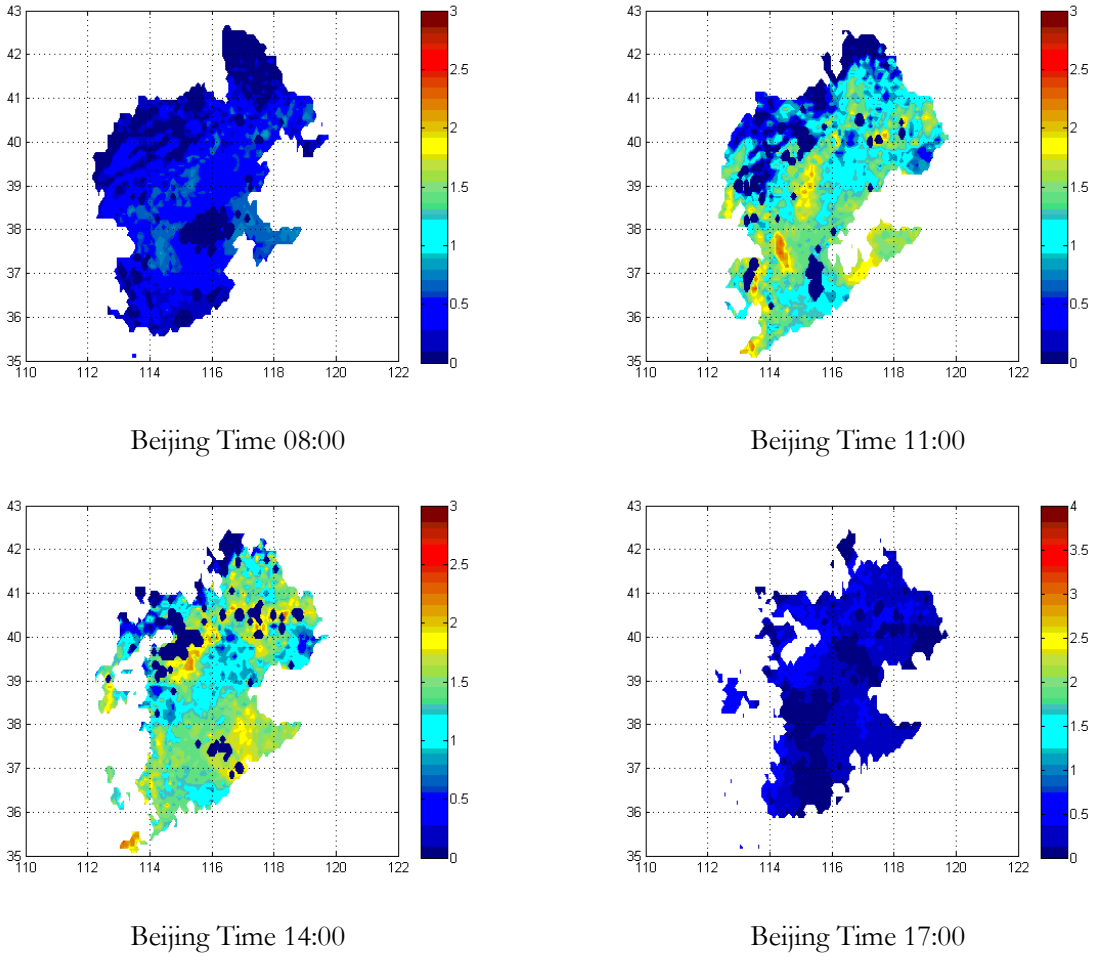

Beijing Time 08:00 Beijing Time 11:00

Beijing Time 14:00 Beijing Time 17:00

Figure 6-12 Hourly ET maps for Haihe River Basin on 12 September 2010 (mm/3h)

For the spatial distribution of evapotranspiration, the daily evapotranspiration can provide the information of distribution clearly. As can be seen from the daily ET maps, higher evapotranspiration is observed in the east, decreases from east to west and from south to north in Haihe River Basin. The high-value areas are mainly concentrated in the northern and eastern which near coastal areas in study area. In the northern area, the terrain is high and the soil moisture is sufficient due to high vegetation coverage, thus the evapotranspiration is higher than other area.

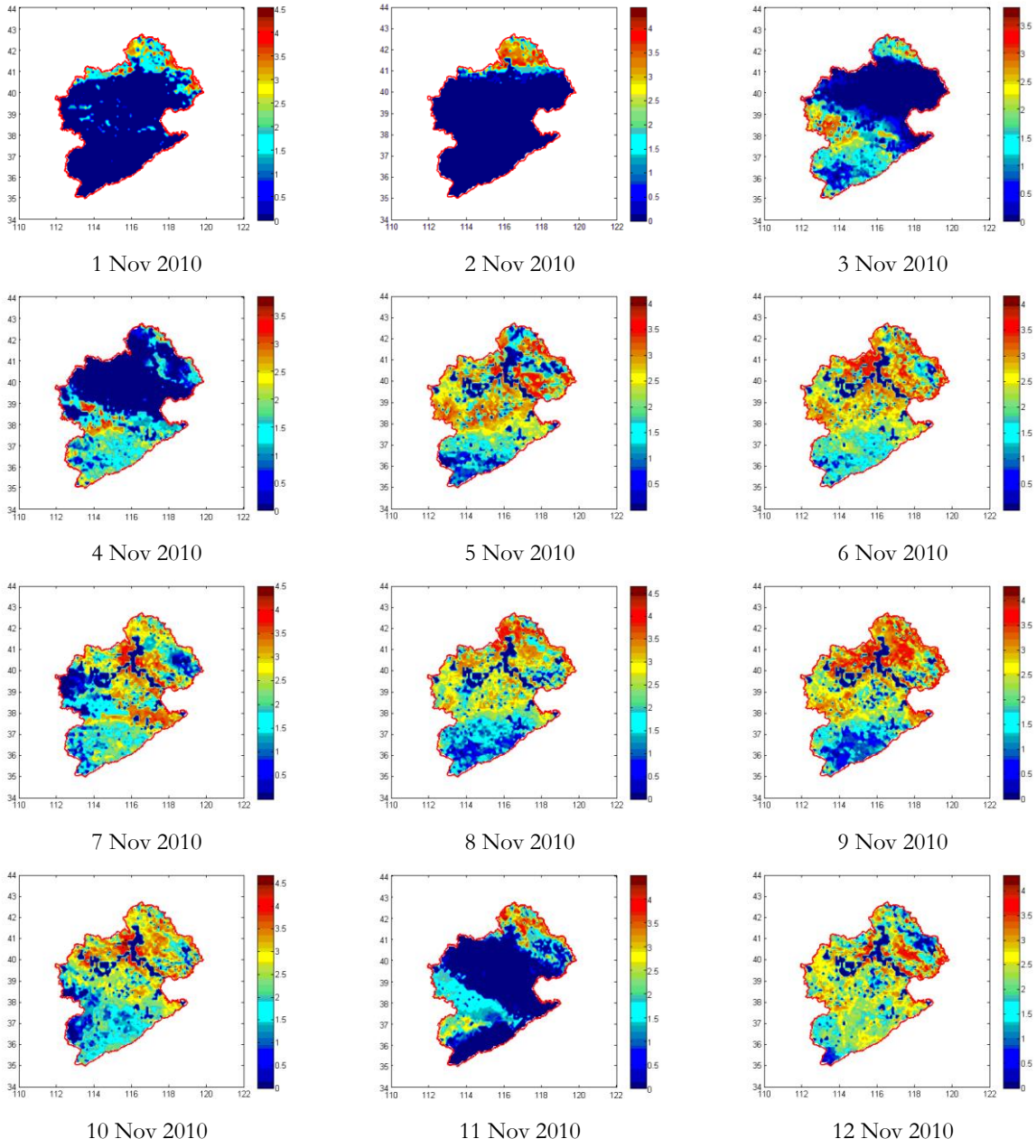

Figure 6-13 Daily maps for Haihe River Basin (mm/d)

Some of figures in Figure 6-13 are shown regions with ET value equal to 0 (such as 1 Nov 2010, 2 Nov 2010 and 11 Nov 2010). The daily evapotranspiration calculated by eight 3-hour map for each day in this study, the null value for each map is assumed to be zero to avoid calculation errors. Therefore, the area occupied by low ET value may means that the hourly map for that day has many null values. Figure 6-14 shown the number of efficient point which used to calculate daily evapotranspiration, the pixel value with 8 represents the daily ET map composite by eight null data. Similarly, the pixel value with 0 represents all of 3-houly data are efficient.

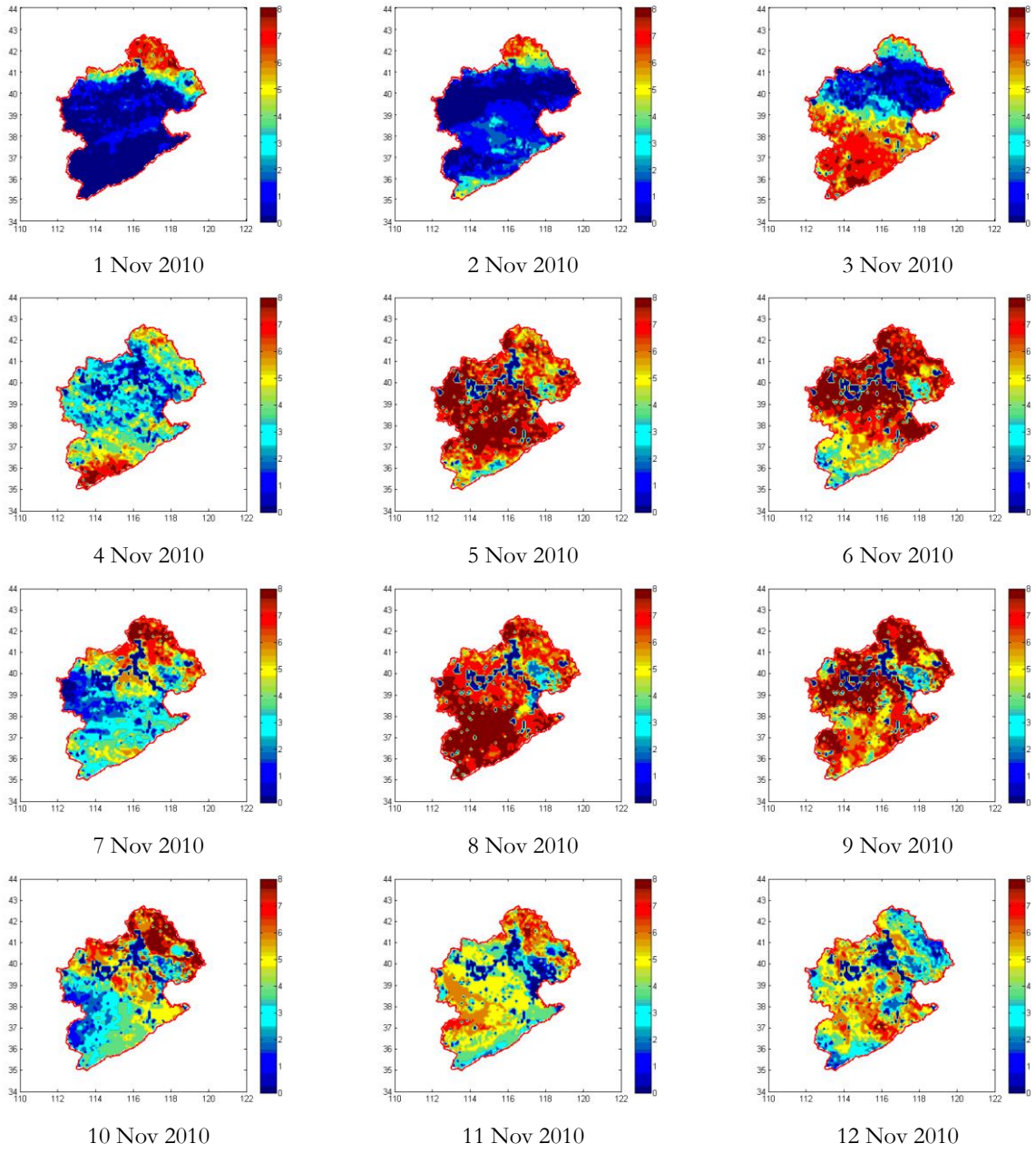

Figure 6-14 The number of efficient point which used to calculate daily evapotranspiration

6.2.3.2. Temporal distribution of daily ET

Evapotranspiration is closely related to temperature and NDVI. As we can see from Figure 6-15. Evapotranspiration in the overall performance: the highest daily transpiration was in summer, followed by spring, then autumn and winter was lowest. From April to June, high evapotranspiration is observed in study area, this occurs because there is large area of cultivated land in the study area, agricultural irrigation produced evapotranspiration during this period. The annual distribution of actual evapotranspiration in the Haihe River Basin has obvious double-peak characteristics. The two peaks appeared in May and August respectively, and a low value appeared in June. Compared this distribution map to other research (Pan et al., 2016), indicated this yearly ET distribution result is reliable.

The annual distribution of actual evapotranspiration reflects the distribution of natural climate conditions and field management system in Haihe River Basin during the whole year. The permafrost period of the Haihe River Basin starts from November to next February. During this period, the effective soil content is low, the winter crops are in a dormant stage, cropland cultivated single-crop is in the bare soil state, and combined with lower land surface temperature limits evaporation capacity, thus evapotranspiration during this period is maintained at a low level. In March, the snow began to melt and replenish soil water. The physiological activities of crops and vegetation began to recover, and the evapotranspiration increased significantly. April and May were crop growth period and main irrigation period in Haihe River Basin. During this period, actual daily evapotranspiration was large because of the sufficient soil water supply and large crop water consumption. June is the harvest period for the crop (winter wheat), the croplands which accounting for 50% of the total area of the Haihe River Basin showed a bare state, daily evapotranspiration decreased slowly. Haihe River Bain into the rainy season in July and August, and the second peak of daily evapotranspiration in the Haihe River Basin observed during this period due to the growth of the second season crop (summer maize) and vegetation, as well as the sufficient heat conditions in summer. Since then, with the changes of hydrothermal conditions and physiological of vegetation, basin evapotranspiration gradually reduced until November, into the frozen period again, completed a cycle
.

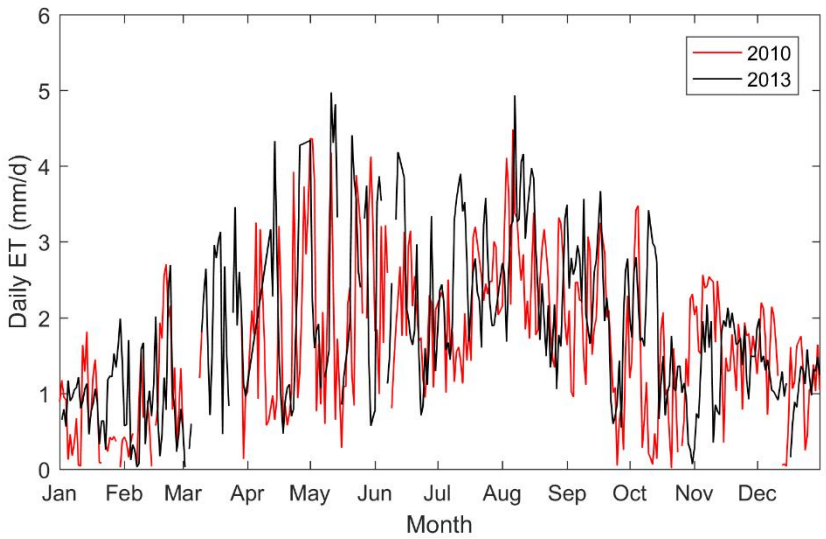

Figure 6-15 Temporal distribution of daily ET

6.2.4. Daily variation analysis

The estimation of hourly evapotranspiration can be used to the research related to ecological environment protection and utilization of water resources reasonable development. The daily variation has been analyze in this study which is essential for studies on climate change and water resource issues. To obtain daily variation of evapotranspiration, we calculated the mean value for each time. This study selected 10 days in different months to calculate the average evapotranspiration, representing four seasons respectively- Winter (1 January ~10 January 2010), Spring (1 April ~10 April 2010), summer (10 July ~20 July 2010), autumn (1 October ~ 10 October 2010). Figure 6-16 shows the daily variation of evapotranspiration over different season (Spring, summer, autumn as well as winter).

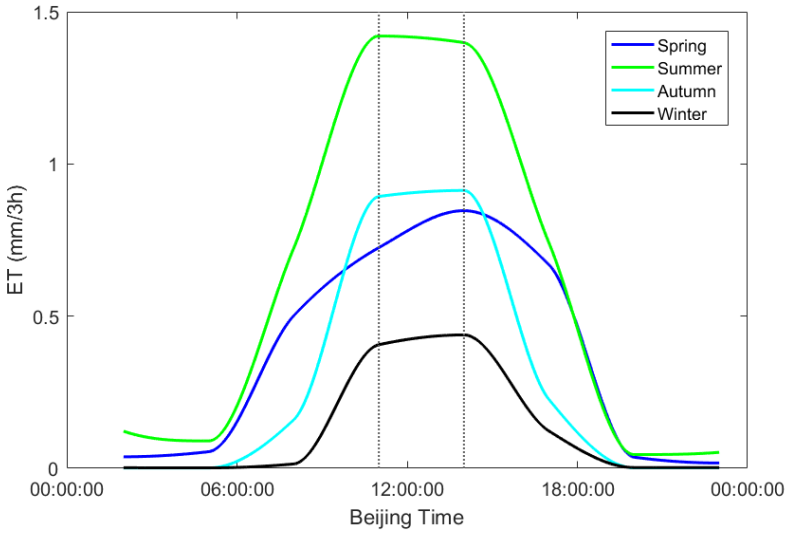

Figure 6-16 Daily variation of ET over different season

It can be seen from the figure, evapotranspiration at all season reached a peak during midday, and bottomed out at night. During the summer, evapotranspiration has a high point at 11:00, then gradually decreased, and daily variation of evapotranspiration was the largest compared to other seasons. The trend of evapotranspiration in spring and autumn is similar, daily variation of evapotranspiration in autumn larger than spring because temperature difference of morning and night is bigger relatively. During winter, the evapotranspiration showed slowly-varying.

6.3. ET Influence factor analysis

6.3.1. Land cover

Based on the understanding of land cover types in the study area, classification will be made by combining MOD12 data IGBP land cover classification scheme which indicated in 4.1.4. In order to do statistics calculation conveniently, we set code 0 is water; Cover type of code 1~5 is uniformly set to 'Forest' (The pixels of evergreen broadleaf forest and deciduous needleleaf forest equal to 0 among them); Cover type of code 6~10 is uniformly set to 'Grassland and wetlands' (The pixels of open shrublands, woody savannas as well as savannas equal to 0 among them); Set code 12 is croplands; Coverage type of code 13~14 is uniformly set to 'Urban'; And cover type of code 15~16 is uniformly set to 'Barren' (The pixels of snow and ice equal to 0 among them). The detail information is shown in Table 6-2.

Table 6-2 Statics land cover classification from MCD12Q1 in the Haihe River Basin

Type	Percentage	Code	Land cover	Pixels	Percentage
Water	0.57%	0	Water	76	0.58%
Forest	7.85%	1	Evergreen Needleleaf forest	96	0.73%
		2	Evergreen Broadleaf forest	0	0
		3	Deciduous Needleleaf forest	6	0.04%
		4	Deciduous Broadleaf forest	81	0.61%
		5	Mixed forest	870	6.58%
Grassland and wetlands	36.18%	6	Closed shrublands	640	4.84%
		7	Open shrublands	5	0.04%
		8	Woody savannas	68	0.51%
		9	Savannas	4	0.03%
		10	Grasslands	4130	30.79%
		11	Permanent wetlands	6	0.04%
Croplands	51.02%	12	Croplands	6842	51.02%
Urban	4.09%	13	Urban and built-up	500	3.73%
		14	Cropland/Natural vegetation mosaic	49	0.37%
Barren	0.29%	15	Snow and ice	0	0
		16	Barren or sparsely vegetated	39	0.29%

This table illustrates that the main vegetation cover types in Haihe River Basin are broadly divided into croplands, grasslands as well as forest. The proportion of croplands was the largest, which is approximately 51% of area, this type has 6842 pixels. Followed by grassland and wetlands, the grassland occupied the largest area in this type, there is 4130 pixels, accounting for the total area of the study area of 30.79%. The third category is the forest, account for 7.85% of total area.

Different types of land cover types have different evapotranspiration capacities due to the physical and chemical properties of the underlying surface are different as the vegetation cover condition as well as soil moisture can also play a role. The evapotranspiration over various land cover types in the study area was statistically analyze for each day in 2010, the detailed contents of statistics are shown in Table 6-3, which represents the average level of evapotranspiration of various land types.

Table 6-3 Mean daily evapotranspiration of different land cover (mm/day) in 2010

Land cover	Water	Forest	Grassland and wetlands	Croplands	Urban	Barren
ET	1.0600	0.8204	0.8375	0.7935	0.7127	1.0196
StDev	0.6390	0.4837	0.5365	0.4791	0.5635	0.6048

As can be seen from the table, the distribution of evapotranspiration in Haihe River Basin has a well consistency with land cover type. The maximum value of evapotranspiration in the study area appeared in the area covered by water and barren where have a strong the evaporation capacity. The land cover type of barren in the study area located mainly close to the coast. The high value of evapotranspiration for barren was due to evapotranspiration mainly comes from the ocean.

The maximum evapotranspiration except water in the study area was found in the woodland-covered area. The woodland area, was covered with a large number mixed forests, and the vegetation coverage was higher than other regions in study area. The higher ET is because of the large evaporation coefficient of forest land, and high level soil moisture maintained due to and abundant rainfall in summer.
Cropland is the most widely distributed land use type in Haihe River Basin, the daily evapotranspiration of cropland was approximately 0.81 mm per day. The evapotranspiration of agricultural land is mainly the result of the combination of meteorological factors, soil moisture conditions, crop characteristics and agricultural technical measures.

Although grassland and wetland is the main vegetation cover in the study area, however, most of the area is grassland with lower vegetation coverage compared to croplands, and weak vegetation transpiration and serious soil and water loss led to the soil moisture is low. The study area is distributed Beijing, Tianjin and Shijiazhuang as well as other counties and cities. The underlying surface of the construction land is mostly impermeable surface, the water in the process of evaporation by a certain resistance, and thus the amount of evapotranspiration is not very high.

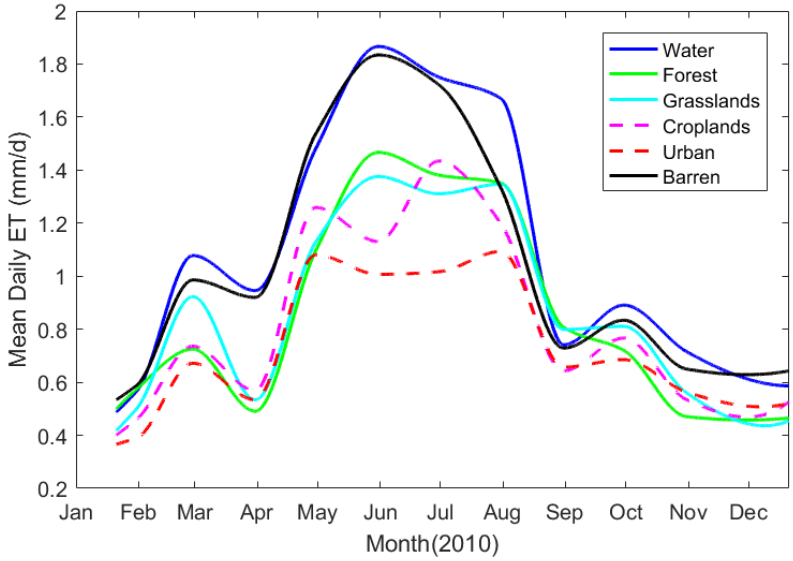

Figure 6-17 Time-series of mean daily ET over different land cover type

Besides, this study also calculated the mean daily evapotranspiration for each month, Figure 6-17 is a curve graph which describes the trend of mean daily evapotranspiration over different land cover type. From the figure, we can see clearly that evapotranspiration is mainly concentrated in June to October. Water has great evapotranspiration variation; On the contrary, the evapotranspiration variation in urban area is small. The evapotranspiration trend in forest, grass and croplands is similar, the croplands has double-peak because of the irrigation in May.

6.3.2. Vegetation (NDVI)

Th value of NDVI also influences evapotranspiration in Haihe River Basin. This paper taken 30th May 2013 as an example, discussed the relationship between evapotranspiration and NDVI. The following figure shows the spatial distribution of NDVI and daily ET, the high value mainly concentrated in the mountainous area, and the low NDVI mainly distributed in city (Beijing, Tianjin and Shijiazhuang) (Figure 6-18). From these two graphs, can be seen that the high surface evapotranspiration located the area where the value of NDVI is high. The mountainous area in the northern part of the study area was covered with forest extensively. During this period, the rainfall was adequate and the soil moisture was high, the NDVI was more than 0.7 because of flourishing plant.

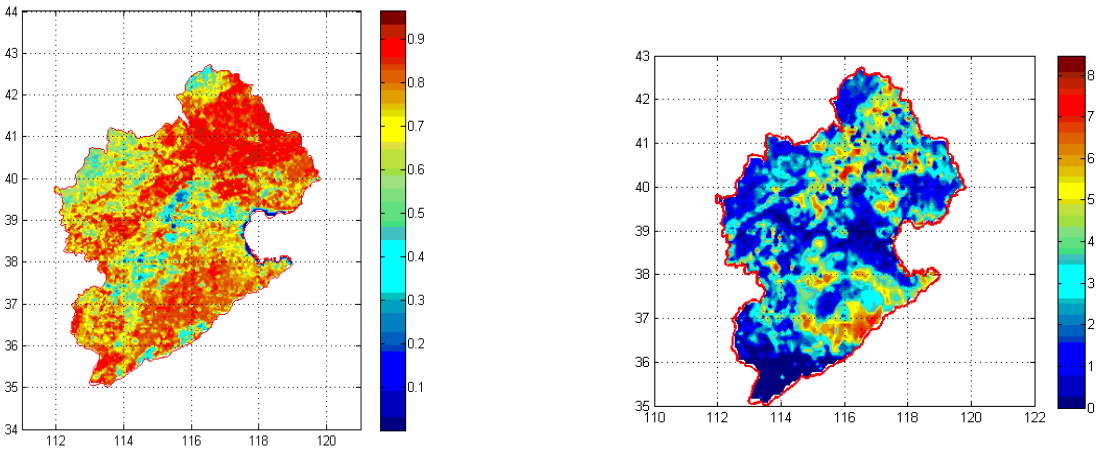

Figure 6-18 The spatial distribution of NDVI (left) and evapotranspiration (right) (30 May 2013)

In order to obtain the specific relationship between the surface evapotranspiration and NDVI, the calculated evapotranspiration based on SEBS model were spatial overlaid with MODIS NDVI data. The NDVI value were divided into 0.05 as a step, calculated the average daily evapotranspiration which represent the vegetation growth condition within the range (Table 6-4).

Table 6-4 Average daily ET for each NDVI domain (mm/d)

Range of NDVI	0~0.05	0.05~0.10	0.10~0.15	0.15~0.20	0.20~0.25
Average daily ET	3.74	2.40	2.16	2.19	2.06
StDev	1.57	1.89	1.68	1.15	1.29
Range of NDVI	0.25~0.30	0.30~0.35	0.35~0.40	0.40~0.45	0.45~0.50
Average daily ET	1.74	1.94	1.99	2.44	2.58
StDev	1.18	1.26	1.22	1.46	1.36
Range of NDVI	0.50~0.55	0.55~0.60	0.60~0.65	0.65~0.70	0.70~0.75
Average daily ET	2.83	3.12	3.35	3.94	4.33
StDev	1.43	1.43	1.49	1.42	1.58
Range of NDVI	0.75~0.80	0.80~0.85	0.85~0.90	0.90~0.95	
Average daily ET	4.60	4.84	4.95	5.15	
StDev	1.48	1.57	1.62	1.52	

From the relationship graph (Figure 6-19) between the evapotranspiration and the NDVI, we can see that the relationship can divided into three sections: evapotranspiration fluctuates with the change of NDVI when NDVI is between 0 and 0.3; The daily evapotranspiration was reached the bottom when NDVI equal to 0.3. When the NDVI is more than 0.3, the NDVI increases along with the increasing vegetation coverage. The transpiration of the plant becomes the main part of the evapotranspiration at this time, and shown an obvious positive correlativity between NDVI and evapotranspiration; The growth of surface evapotranspiration tends to be slow when NDVI remained more than 0.83.

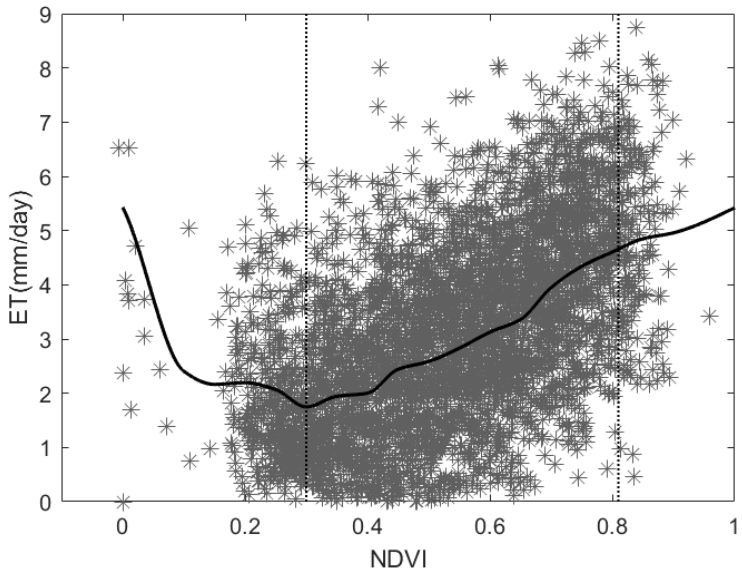

Figure 6-19 Relation curve of evapotranspiration and NDVI (30 May 2013)

Based on the principle of NDVI, the greater the NDVI with the vegetation cover is better. In fact, it assumes that it has a linear relation between NDVI and vegetation fraction f_c. However, the relationship not like this under real condition. The result of a previous study (Fan & Zhang, 2010; Todd & Hoffer, 1998) show that the value of NDVI is sensitive to soil back ground. When the vegetation fraction is less than 15%, the vegetation which NDVI value is higher than the bare soil can be detected. In the area with low vegetation fraction (such as arid, semi-arid areas), however, NDVI is difficult to indicate the local plant biomass condition (called 'invalid NDVI' in here). The NDVI value is linear to plant biomass when the vegetation coverage increasing from 25% to 80%. Next, the sensitivity of NDVI to vegetation will decrease when vegetation fraction larger than 80%. It can be seen from Figure 6-2, maximum value of NDVI is 0.97, and minimum value of NDVI is 0.03. Therefore, it can be decided that the NDVI equal to 0.27 and 0.80 when f_c is 25% and 80% respectively according Equation (4-2).

From what has been discussed above we may safely draw the conclusion that: the pixel represent water when NDVI lower than 0, daily evapotranspiration is about 5.5 mm. When the NDVI is less than 0.29, the daily evapotranspiration fluctuates with the vegetation index due to the "mixed pixel" effect and 'invalid NDVI'. The proportion of vegetation is gradually increased when NDVI increasing from 0.29 to 0.81, as well as the evapotranspiration also increases rapidly. When NDVI lager than 0.81, NDVI present saturation state and the increase rate of evapotranspiration was slow down

6.3.3. Climate

Evapotranspiration is affected by the radiation from the sun, wind speed, temperature and relative humidity and other climate factors. This study selected the study area precipitation data of Huailai weather station in 2013, compared daily evapotranspiration and precipitation in time series as is shown in the Figure 6-20. As can be seen from the figure, the peak value of precipitation most happens in June to September, and the maximum of evapotranspiration occurred in April to July. The difference between the peak time of the precipitation and the evapotranspiration is about two months. Meantime, daily evapotranspiration is much greater than the rainfall at same year, this phenomenon exacerbates the degree of drought in the Haihe River Basin, resulting in typical "spring drought" phenomenon in the study area.

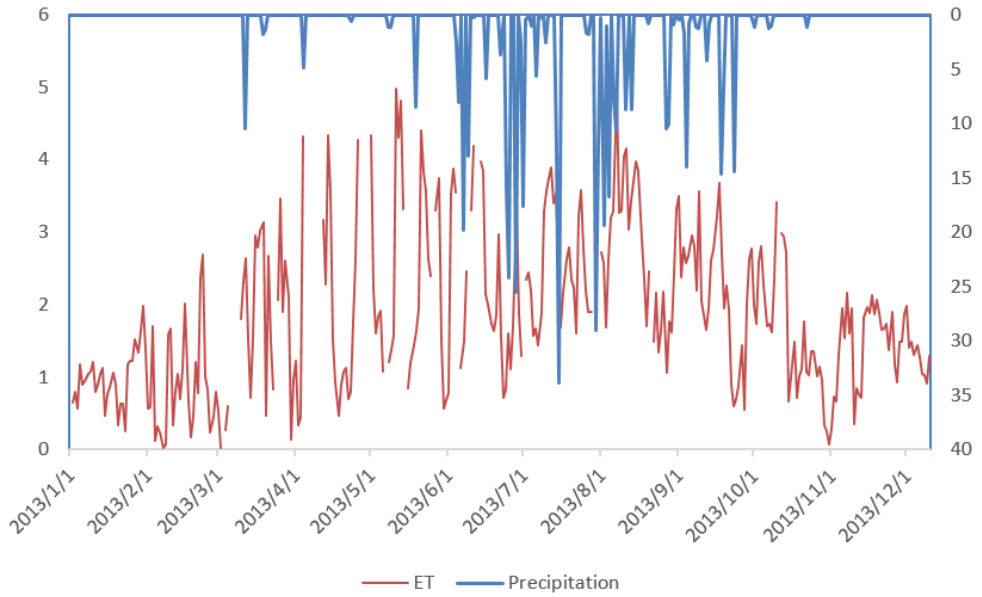

Figure 6-20 Comparison of evapotranspiration and precipitation in time series

6.4. ET error source analysis

6.4.1. The influence of geographical location

The study area is located along the coast, with vast area, complicated topography and variable climate. In the meantime, there are several cities such as Beijing and Tianjin in this basin, which results in the difference of the surface characteristic parameters and meteorological data. The elevation of this area ranges from 0 to 2000 m, and the range of meteorological data varies greatly with elevation. This research using 0.1° forcing dataset, however, the spatial resolution is difficult to express accurately the terrain changes within a pixel.

6.4.2. Meteorological data

Meteorological data used to this study is ITPCAS forcing data. The meteorological forcing data was produced by merging a variety of data such as CMA data, TRMM satellite precipitation analysis data, GEWEX-SRB data, Princeton forcing data and GLDAS data from ground observation and reanalysis. Although it is more accurate than other forcing data sets as indicated in Section 4.1.2, this data also have some errors which influence the result of SEBS output. This dataset was interpolated; however, the study area is large, these information can not represent the characteristics of the entire atmospheric boundary layer, especially in the area with greatly undulate terrain. This causes the phenomenon that the surface

temperature is non-zero while the evaporation fraction is zero. In addition, there are some errors in the process that the observation data interpolation to the satellite transit time

6.4.3. Error of LST data

The land surface temperature data with high resolution was derived from geostationary satellite MTSAT. It is only can obtained during the free-cloud weather, affected by the cloud and likely to cause the data gap. For this research, the hourly ET map was selected from the moment with free-clouds. In the case of full clouds, it is assumed that the evapotranspiration in the area equal to zero.

7. CONCLUSIONS AND RECOMMENDATIONS

7.1. Conclusions

The main objective of this research is to generate actual hourly and daily evapotranspiration and evaluate the spatial as well as temporal distribution using remote sensing technology and meteorological forcing dataset in Haihe River basin. For this propose, some satellite and forcing data sets were download from the free website, as well as in-situ data were collected during the fieldwork. This study used the SEBS model which is based on the surface energy balance system realized remote sensing estimation of evapotranspiration by MATLAB programing. In addition, this study attempt four parameterized method to obtained better result.

This research describes the situation in the study area, including the geography, climate, vegetation in Haihe River Basin, show that the situation of water resources in this region is more serious. Therefore, the high temporal resolution land heat flux maps are necessary in this area. To sum up, the R^2 is equal to 0.67 indicated 3 hourly and daily evapotranspiration derived from SEBS model performed well in study area, the estimation for high temporal resolution evapotranspiration using remote sensing method is feasible. And the results of the model are close to the average evapotranspiration of the related literature. It is further proved that the SEBS model is reasonable and accurate Finally, the influence factor for SEBS evapotranspiration and possible error sources were also pointed out based on the result of this study.

In general, it can be obtained high temporal land surface temperature using MTSAT satellite data. As an attempt and exploration to apply SEBS model to high temporal resolution, this study estimated 3-hourly and daily evapotranspiration using SEBS model, results are good relatively by compared with in-situ observations and similar study.

7.2. Recommendations

In this paper, the SEBS model and geostationary satellite are used to estimate the hourly and daily evapotranspiration of the Haihe River Basin. The temporal and spatial distribution characteristics of surface parameters, radiation, latent heat flux and evapotranspiration has been analysed, then final results have been validated and analysed. The following aspects need to be strengthen in the future:

1. To further strengthen the understanding and mastery of evapotranspiration model using remote sensing technology. SEBS model has been widely used as one of the more accurate models. The key of this research is mastery of principle, I should have targeted learning the model-related knowledge.

2. To further study on parameterization of model intensively. In the calculation of evapotranspiration using remote sensing techniques, each process has problems about accuracy of parameter from the observed data to the remote sensing data and the acquisition of land surface parameters.

3. The issues about optimization and validation of results. The hourly and daily evapotranspiration estimated from the remote sensing model should be compared with the in-situ measurement data to verify its accuracy and reliability. The observed values obtained at the point cannot effectively test the average evapotranspiration on each pixel obtained from remote sensing data.

4. Application of high spatial resolution satellite data to reduce the space scale error. High temporal resolution satellites have a lower spatial resolution because of the limitations of remote sensing technology. In the future, we can take advantage of the method that combine high temporal resolution and high spatial resolution satellite data to energy balance research.

LIST OF REFERENCES

Abtew, W., & Melesse, A. (2013). *Evaporation and Evapotranspiration Measurement*. *Evaporation and Evapotranspiration: Measurements and Estimations* (1st ed.). Dordrecht: Springer Netherlands. https://doi.org/10.1007/978-94-007-4737-1

Agency Japan Meteorological. (2008). Meteorological Satellites -Japan Meteorological Agency. Retrieved August 18, 2016, from http://www.jma.go.jp/jma/jma-eng/satellite/introduction/MTSAT_series.html#05

Allen, R. G., Tasumi, M., & Trezza, R. (2007). Satellite-based energy balance for mapping evapotranspiration with internalized calibration (METRIC) – Model. *Journal of Irrigation and Drainage Engineering*, *133*(4), 395–406. https://doi.org/10.1061/(ASCE)0733-9437(2007)133:4(395)

Amisigo, B., McCluskey, A., & Swanson, R. (2015). Modeling Impact of Climate Change on Water Resources and Agriculture Demand in the Volta Basin and other Basin Systems in Ghana. *Sustainability*, *7*(6), 6957–6975. https://doi.org/10.3390/su7066957

Anderson, M. C., Norman, J. M., Diak, G. R., Kustas, W. P., & Mecikalski, J. R. (1997). A two-source time-integrated model for estimating surface fluxes using thermal infrared remote sensing. *Remote Sensing Of Environment*, *60*(2), 195–216. https://doi.org/10.1016/s0034-4257(96)00215-5

Angstrom, A. (1925). The Albedo of Various Surfaces of Ground. *Geografiska Annaler*, *7*, 323–342. https://doi.org/10.2307/519495

Baik, J., & Choi, M. (2015). Evaluation of geostationary satellite (COMS) based Priestley-Taylor evapotranspiration. *Agricultural Water Management*, *159*, 77–91. https://doi.org/10.1016/j.agwat.2015.05.017

Bastiaanssen, W. G. M., Menenti, M., Feddes, R. A., & Holtslag, A. A. M. (1998). A remote sensing surface energy balance algorithm for land (SEBAL): 1. Formulation. *Journal of Hydrology*, *212–213*(1–4), 198–212. https://doi.org/10.1016/S0022-1694(98)00253-4

Becker, F., & Li, Z. L. (1990). Toward a local split window method over land surface. *Int. J. Remote Sens.* https://doi.org/10.1080/01431169008955028

Betts, A. K., & Ball, J. H. (1997). Albedo over the boreal forest. *Journal of Geophysical Research: Atmospheres*, *102*(D24), 28901–28909. https://doi.org/10.1029/96JD03876

Bhantana, P., & Lazarovitch, N. (2010). Evapotranspiration, crop coefficient and growth of two young pomegranate (Punica granatum L.) varieties under salt stress. *Agricultural Water Management*, *97*(5), 715–722. https://doi.org/10.1016/j.agwat.2009.12.016

Bhattarai, N., Shaw, S. B., Quackenbush, L. J., Im, J., & Niraula, R. (2016). Evaluating five remote sensing based single-source surface energy balance models for estimating daily evapotranspiration in a humid subtropical climate. *International Journal of Applied Earth Observation and Geoinformation*, *49*, 75–86. https://doi.org/10.1016/j.jag.2016.01.010

Brutsaert, W. (1982). Evaporation into the Atmosphere Theory, History and Applications. Dordrecht: Springer Netherlands. Retrieved from http://dx.doi.org/10.1007/978-94-017-1497-6

Chahine, M. T. (1992). The hydrological cycle and its influence on climate. *Nature*, *359*(6394), 373–380.

Chen, X., Su, Z., Ma, Y., Liu, S., Yu, Q., & Xu, Z. (2014). Development of a 10-year (2001-2010) 0.1?? data set of land-surface energy balance for mainland China. *Atmospheric Chemistry and Physics*, *14*(23), 13097–13117. https://doi.org/10.5194/acp-14-13097-2014

Chen, X., Su, Z., Ma, Y., Yang, K., & Wang, B. (2013). Estimation of surface energy fluxes under complex terrain of Mt. Qomolangma over the Tibetan Plateau. *Hydrology and Earth System Sciences*, *17*(4), 1607–1618. https://doi.org/10.5194/hess-17-1607-2013

Chen, X., Su, Z., Ma, Y., Yang, K., Wen, J., & Zhang, Y. (2013). An improvement of roughness height parameterization of the Surface Energy Balance System (SEBS) over the Tibetan plateau. *Journal of Applied Meteorology and Climatology*, *52*(3), 607–622. https://doi.org/10.1175/JAMC-D-12-056.1

Chen, Y., Yang, K., He, J., Qin, J., Shi, J., Du, J., & He, Q. (2011). Improving land surface temperature modeling for dry land of China. *Journal of Geophysical Research Atmospheres*, *116*(20), 1–15. https://doi.org/10.1029/2011JD015921

Cho, H., Ho, C. H., & Choi, Y. S. (2012). The observed variation in cloud-induced longwave radiation in response to sea surface temperature over the Pacific warm pool from MTSAT-1R imagery. *Geophysical Research Letters*, *39*(17), 1–6. https://doi.org/10.1029/2012GL052700

Choudhury, B. J., & Monteith, J. L. (1988). A four-layer model for the heat budget of homogeneous land surfaces. *Quarterly Journal of the Royal Meteorological Society*, *114*(480), 373–398. https://doi.org/10.1002/qj.49711448006

Cleugh, H. A., Leuning, R., Mu, Q., & Running, S. W. (2007). Regional evaporation estimates from flux tower and MODIS satellite data. *Remote Sensing of Environment*, *106*(3), 285–304. https://doi.org/10.1016/j.rse.2006.07.007

Fan, J., & Zhang, X. (2010). Study on the vegetation dynamic change using long time series of remote sensing data. *Proceedings of SPIE - The International Society for Optical Engineering*, *7824*, 1–6. https://doi.org/10.1117/12.864670

Freitas, S. C., Trigo, I. F., Macedo, J., Silva, R., & Perdigão, R. (2013). Land surface temperature from multiple geostationary satellites. *International Journal of Remote Sensing*, *34*(9–10), 3051–3068. https://doi.org/10.1080/01431161.2012.716925

Gao, G., Xu, C.-Y., Chen, D., & Singh, V. P. (2012). Spatial and temporal characteristics of actual evapotranspiration over Haihe River basin in China. *Stochastic Environmental Research and Risk Assessment*, *26*(5), 655–669. https://doi.org/10.1007/s00477-011-0525-1

Guo, Y., & Shen, Y. (2015). Quantifying water and energy budgets and the impacts of climatic and human factors in the Haihe River Basin, China: 1. Model and validation. *Journal of Hydrology*, *528*, 206–216. https://doi.org/10.1016/j.jhydrol.2015.06.039

Hargreaves, G. H., & Samani, Z. A. (1982). Estimating potential evapotranspiration. *Journal of the Irrigation and Drainage Division*, *108*(3), 225–230.

He, J., & Yang, K. (2011). China Meteorological Forcing Dataset. *Cold and Arid Regions Science Data Center at Lanzhou*. https://doi.org/doi:10.3972/westdc.002.2014.db

Holdridge, L. R. (1959). Simple method for determining potential evapotranspiration from temperature data. *Science*, *130*(3375), 572.

Howell, T. A. (2001). Enhancing water use efficiency in irrigated agriculture. *Agronomy Journal*, *93*(2), 281–289.

Huang, G., Ma, M., Liang, S., Liu, S., & Li, X. (2011). A LUT-based approach to estimate surface solar irradiance by combining MODIS and MTSAT data. *Journal of Geophysical Research Atmospheres*, *116*(22), 1–14. https://doi.org/10.1029/2011JD016120

Idso, S., & Jackson, R. (1975). The dependence of bare soil albedo on soil water content. *Journal of Applied Meteorology and Climatology*. https://doi.org/10.1175/1520-0450(1975)014<0109:TDOBSA>2.0.CO;2

Jia, L., Su, Z., van den Hurk, B., Menenti, M., Moene, A., De Bruin, H. A. R., … Cuesta, A. (2003). Estimation of sensible heat flux using the Surface Energy Balance System (SEBS) and ATSR measurements. *Physics and Chemistry of the Earth*, *28*(1–3), 75–88. https://doi.org/10.1016/S1474-7065(03)00009-3

Jia, Y., Wang, H., Gan, H., Zhou, Z., Qiu, Y., You, J., … Niu, C. (2009). Development of Dualistic Model for Integrated Water Resources Management in the Haihe River Basin. *Advances in Water Resources and Hydraulic Engineering, Vols 1-6*, (50721006), 281–287. https://doi.org/Doi 10.1007/978-3-540-89465-0_52

Jia, Z., Liu, S., Xu, Z., Chen, Y., & Zhu, M. (2012). Validation of remotely sensed evapotranspiration over the Hai River Basin, China. *Journal of Geophysical Research Atmospheres*, *117*(13), 1–21. https://doi.org/10.1029/2011JD017037

Jung, M., Reichstein, M., Ciais, P., Seneviratne, S. I., Sheffield, J., Goulden, M. L., … Zhang, K. (2010). Recent decline in the global land evapotranspiration trend due to limited moisture supply. *Nature*, *467*(7318), 951–954. https://doi.org/10.1038/nature09396

Kawamura, H., Qin, H., Sakaida, F., & Setiawan, R. Y. (2010). Hourly sea surface temperature retrieval using the Japanese geostationary satellite, Multi-functional Transport Satellite (MTSAT). *Journal of Oceanography*, *66*(1), 61–70. https://doi.org/10.1007/s10872-010-0005-0

Kim, J. H., & Suh, M. seok. (2011). Development of Land Surface Temperature Retrieval Algorithm from the MTSAT-2 Data, *27*(6), 653–662.

Kim, M. J., Ou, M.-L., Sohn, E. H., & Kim, Y. (2011). Characteristics of sea surface temperature retrieved from MTSAT-1R and in-situ data. *Asia-Pacific Journal of Atmospheric Sciences*, *47*(5), 421–427. https://doi.org/10.1007/s13143-011-0027-6

Liu, C., Zhang, X., & Zhang, Y. (2002). Determination of daily evaporation and evapotranspiration of winter wheat and maize by large-scale weighing lysimeter and micro-lysimeter. *Agricultural and Forest Meteorology*, *111*(2), 109–120. https://doi.org/10.1016/S0168-1923(02)00015-1

Liu, R., Wen, J., Wang, X., & Zhang, Y. (2015). Evapotranspiration estimated by using datasets from the Chinese FengYun-2D geostationary meteorological satellite over the Yellow River source area. *Advances in Space Research*, *55*(1), 60–71. https://doi.org/10.1016/j.asr.2014.09.018

Liu, S., Xu, Z., Zhu, Z., Jia, Z. Z., & Zhu, M. J. (2013). Measurements of evapotranspiration from eddy-covariance systems and large aperture scintillometers in the Hai River Basin, China. *Journal of Hydrology*, *487*, 24–38. https://doi.org/10.1016/j.jhydrol.2013.02.025

Liu, S., Yan, D., Wang, H., Li, C., Weng, B., & Qin, T. (2016). Standardized Water Budget Index and Validation in Drought Estimation of Haihe River Basin , North China, *2016*.

Ma, W., Hafeez, M., Ishikawa, H., & Ma, Y. (2013). Evaluation of SEBS for estimation of actual evapotranspiration using ASTER satellite data for irrigation areas of Australia. *Theoretical and Applied Climatology*, *112*(3–4), 609–616. https://doi.org/10.1007/s00704-012-0754-3

Malamos, N., Barouchas, P. E., Tsirogiannis, I. L., Liopa-Tsakalidi, A., & Koromilas, T. (2015). Estimation of Monthly FAO Penman-Monteith Evapotranspiration in GIS Environment, through a Geometry Independent Algorithm. *Agriculture and Agricultural Science Procedia*, *4*, 290–299. https://doi.org/10.1016/j.aaspro.2015.03.033

Mamo, T. A. (2010). *Estimation of Actual Evapotranspiration and Water Balance using Combined Geostationary and Polar Orbiting Satellite Products : A case Study in Spain*. Univesity of Twente.

Massman, W. J. (1997). An analytical one-dimensional model of momentum transfer by vegetation of arbitrary structure. *Boundary-Layer Meteorology*, *83*, 407–421. https://doi.org/10.1023/a:1000234813011

Massman, W. J. (1999). A model study of kB(H/-1) for vegetated surfaces using "localized near-field" Lagrangian theory. *Journal of Hydrology*, *223*(1–2), 27–43. https://doi.org/10.1016/S0022-1694(99)00104-3

Massman, W. J., Forthofer, J., & Finney, M. A. (2017). An Improved Canopy Wind Model for Predicting Wind Adjustment Factors and Wildland Fire Behavior. *Canadian Journal of Forest Research*. https://doi.org/10.1139/cjfr-2016-0354

Menenti, M., & Choudhury, B. J. (1993). Parameterization of land surface evaporation by means of location dependent potential evaporation and surface temperature range. *Proceedings of IAHS Conference on Land Surface Processes*, *0*(212), 561–568.

Migliaccio, K. W., & Barclay Shoemaker, W. (2014). Estimation of urban subtropical bahiagrass (Paspalum notatum) evapotranspiration using crop coefficients and the eddy covariance method. *Hydrological Processes*, *28*(15), 4487–4495. https://doi.org/10.1002/hyp.9958

Norman, J. M., & Becker, F. (1995). Terminology in thermal infrared remote sensing of natural surfaces. *Agricultural and Forest Meteorology*, *77*(3–4), 153–166. https://doi.org/10.1016/0168-1923(95)02259-Z

Oyoshi, K., Akatsuka, S., Takeuchi, W., & Sobue, S. (2015). Hourly LST Monitoring with the Japanese Geostationary Satellite MTSAT-1R over the Asia-Pacific Region.

Pan, Y., Zhang, C., Gong, H., Yeh, P. J.-F., Shen, Y., Guo, Y., … Li, X. (2016). Detection of Human-induced Evapotranspiration using GRACE Satellite Observations in the Haihe River Basin of China. *Geophysical Research Letters*, 190–199. https://doi.org/10.1002/2016GL071287

Penman, H. L. (1948). Natural Evaporation from Open Water, Bare Soil and Grass. *Proceedings of the Royal Society of London. Series A, Mathematical and Physical Sciences*, *193*(1032), 120–145. https://doi.org/10.1017/CBO9781107415324.004

Pidwirny, M. (2006). Atmospheric Effects on Incoming Solar Radiation. Retrieved January 19, 2017, from http://www.physicalgeography.net/fundamentals/7f.html%0A %0A

Planton, S. (2013). Annex III: Glossary, In: Climate Change 2013: The Physical Science Basis. Contribution of Working Group I to the Fifth Assessment Report of the Intergovernmental Panel on Climate Change. *Climate Change 2013: The Physical Science Basis. Contribution of Working Group I to the Fifth Assessment Report of the Intergovernmental Panel on Climate Change*, 1447–1466. https://doi.org/10.1017/CBO9781107415324.031

Rwasoka, D. T., Gumindoga, W., & Gwenzi, J. (2011). Estimation of actual evapotranspiration using the Surface Energy Balance System (SEBS) algorithm in the Upper Manyame catchment in Zimbabwe. *Physics and Chemistry of the Earth*, *36*(14–15), 736–746. https://doi.org/10.1016/j.pce.2011.07.035

Sellers, P. J., Dickinson, R. E., Randall, D. A., Betts, A. K., Hall, F. G., Berry, J. A., … Nobre, C. A. (1997). Modeling the exchanges of energy, water, and carbon between continents and the atmosphere. *Science*, *275*(5299), 502–509.

Sobrino, J. A., Jiménez-Muñoz, J. C., & Paolini, L. (2004). Land surface temperature retrieval from LANDSAT TM 5. *Remote Sensing of Environment*, *90*(4), 434–440. https://doi.org/10.1016/j.rse.2004.02.003

Su, Z. (1996). *Remote sensing applied to hydrology: the Sauer river basin study* (Schriftenreihe Hydrologie - Wasserwirtschaft;15). Ruhr-Universitaet, Bochum.

Su, Z. (2002). The Surface Energy Balance System (SEBS) for estimation of turbulent heat fluxes. *Hydrology and Earth System Sciences*, *6*(1), 85–100. https://doi.org/10.5194/hess-6-85-2002

Su, Z., Pelgrum, H., & Menenti, M. (1999). Aggregation effects of surface heterogeneity in land surface processes. *Hydrology and Earth System Sciences*. https://doi.org/10.5194/hess-3-549-1999

Su, Z., Schmugge, T., Kustas, W. P., & Massman, W. J. (2001). An Evaluation of Two Models for Estimation of the Roughness Height for Heat Transfer between the Land Surface and the Atmosphere. *Journal of Applied Meteorology*, *40*(11), 1933–1951. https://doi.org/10.1175/1520-0450(2001)040<1933:AEOTMF>2.0.CO;2

Thomas, F. (2008). The Energy Balance Closure Problem : An Overview. *Ecological Applications*, *18*(October 2008), 1351–1367. https://doi.org/10.1890/06-0922.1

Thomas, F., Mauder, M., Liebethal, C., Wimmer, F., Beyrich, F., Leps, J. P., … Bange, J. (2010). Energy balance closure for the LITFASS-2003 experiment. *Theoretical and Applied Climatology*, *101*(1), 149–160. https://doi.org/10.1007/s00704-009-0216-8

Thornthwaite, C. W. (1948). An Approach Toward a Rational Classification of Climate. *Soil Science*, *66*(1). https://doi.org/10.1097/00010694-194807000-00007

Todd, W., & Hoffer, M. (1998). Responses of Spectral Indices to Variations in Vegetation Cover and Soil Background. *Photogrammetric Engineering and Remote Sensing*, *64*(9), 915–921.

Tsouni, A., Kontoes, C., Koutsoyiannis, D., & Elias, P. (2008). Estimation of Actual Evapotranspiration by Remote Sensing:, (November), 3586–3600. https://doi.org/10.3390/s8063586

Uddin, J., Hancock, N. H., Smith, R. J., & Foley, J. P. (2013). Measurement of evapotranspiration during sprinkler irrigation using a precision energy budget (Bowen ratio, eddy covariance) methodology. *Agricultural Water Management*, *116*, 89–100. https://doi.org/10.1016/j.agwat.2012.10.008

Wan, L., Zhou, J., Guo, H., Cui, M., & Liu, Y. (2016). Trend of water resource amount, drought frequency, and agricultural exposure to water stresses in the karst regions of South China. *Natural Hazards*, *80*(1), 23–42. https://doi.org/10.1007/s11069-015-1954-9

Wan, Z., Zhang, Q., & Li, L. (2004). Quality assessment and validation of the MODIS global land surface temperature. *International Journal of Remote Sensing*, *25*(November 1999), 261–274. https://doi.org/10.1080/0143116031000116417

Wang, Y., Li, X., & Tang, S. (2013). Validation of the SEBS-derived sensible heat for FY3A/VIRR and TERRA/MODIS over an alpine grass region using LAS measurements. *International Journal of Applied Earth Observation and Geoinformation*, *23*(1), 226–233. https://doi.org/10.1016/j.jag.2012.09.005

Wilson, K. (2002). Energy balance closure at FLUXNET sites. *Agricultural and Forest Meteorology*, *113*(1–4), 223–243. https://doi.org/10.1016/S0168-1923(02)00109-0

Wiscombe, W. J., & Warren, S. G. (1980). A Model for the Spectral Albedo of Snow. I: Pure Snow. *Journal of the Atmospheric Sciences*, *37*(12), 2712–2733. https://doi.org/10.1175/1520-0469(1980)037<2712:AMFTSA>2.0.CO;2

Wong, M., Zhu, R., Liu, Z., Lu, L., Peng, J., Tang, Z., … Chan, W. K. (2016). Estimation of Hong Kong's solar energy potential using GIS and remote sensing technologies. *Renewable Energy*, *99*, 325–335. https://doi.org/10.1016/j.renene.2016.07.003

Wu, B., Zhu, W., Yan, N., Feng, X., Xing, Q., & Zhuang, Q. (2016). An Improved Method for Deriving Daily Evapotranspiration Estimates From Satellite Estimates on Cloud-Free Days. *IEEE Journal of Selected Topics in Applied Earth Observations and Remote Sensing*, *9*(4), 1323–1330.

Xue, B. L., Wang, L., Yang, K., Tian, L., Qin, J., Chen, Y., … Li, X. (2013). Modeling the land surface water and energy cycles of a mesoscale watershed in the central Tibetan Plateau during summer with a distributed hydrological model. *Journal of Geophysical Research Atmospheres*, *118*(16), 8857–8868. https://doi.org/10.1002/jgrd.50696

Yang, K., He, J., Tang, W., Qin, J., & Cheng, C. C. K. (2010). On downward shortwave and longwave radiations over high altitude regions: Observation and modeling in the Tibetan Plateau. *Agricultural and Forest Meteorology*, *150*(1), 38–46. https://doi.org/10.1016/j.agrformet.2009.08.004

Yang, K., Koike, T., Fujii, H., Tamagawa, K., & Hirose, N. (2002). Improvement of surface flux parametrizations with a turbulence-related length. *Quarterly Journal of the Royal Meteorological Society*, *128*(584), 2073–2087. https://doi.org/10.1256/003590002320603548

Yao, Y., Liang, S., Cheng, J., Liu, S., Fisher, J. B., Zhang, X., … Zhao, S. (2013). MODIS-driven estimation of terrestrial latent heat flux in China based on a modified Priestley-Taylor algorithm. *Agricultural and Forest Meteorology*, *171–172*, 187–202. https://doi.org/10.1016/j.agrformet.2012.11.016

Zhan, C., Zhao, J., Wang, H., & Yin, J. (2011). Quantitative estimation of land surface evapotranspiration in Taiwan based on MODIS data. *Water Science and Engineering*, *4*(3), 237–245. https://doi.org/10.3882/j.issn.1674-2370.2011.03.001

Zhang, K., Kimball, J. S., Nemani, R. R., & Running, S. W. (2010). A continuous satellite-derived global record of land surface evapotranspiration from 1983 to 2006. *Water Resources Research*, *46*(9), 1–21. https://doi.org/10.1029/2009WR008800

Zhao, H., Fu, Y. H., Wang, X., Zhao, C., Zeng, Z., & Piao, S. (2016). Timing of rice maturity in China is affected more by transplanting date than by climate change. *Agricultural and Forest Meteorology*, *216*, 215–220. https://doi.org/10.1016/j.agrformet.2015.11.001

Appendix A: Test 1

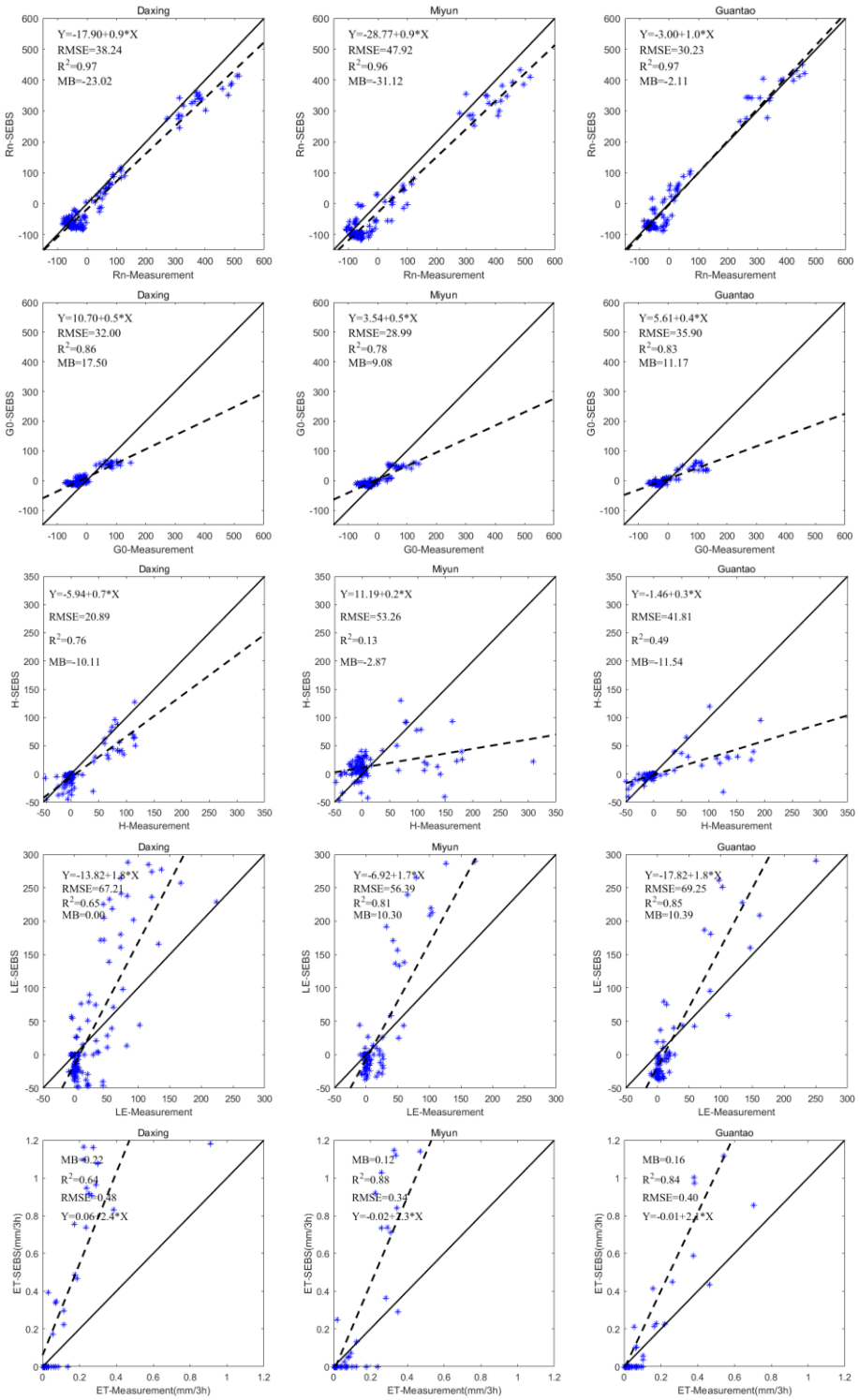

Test2

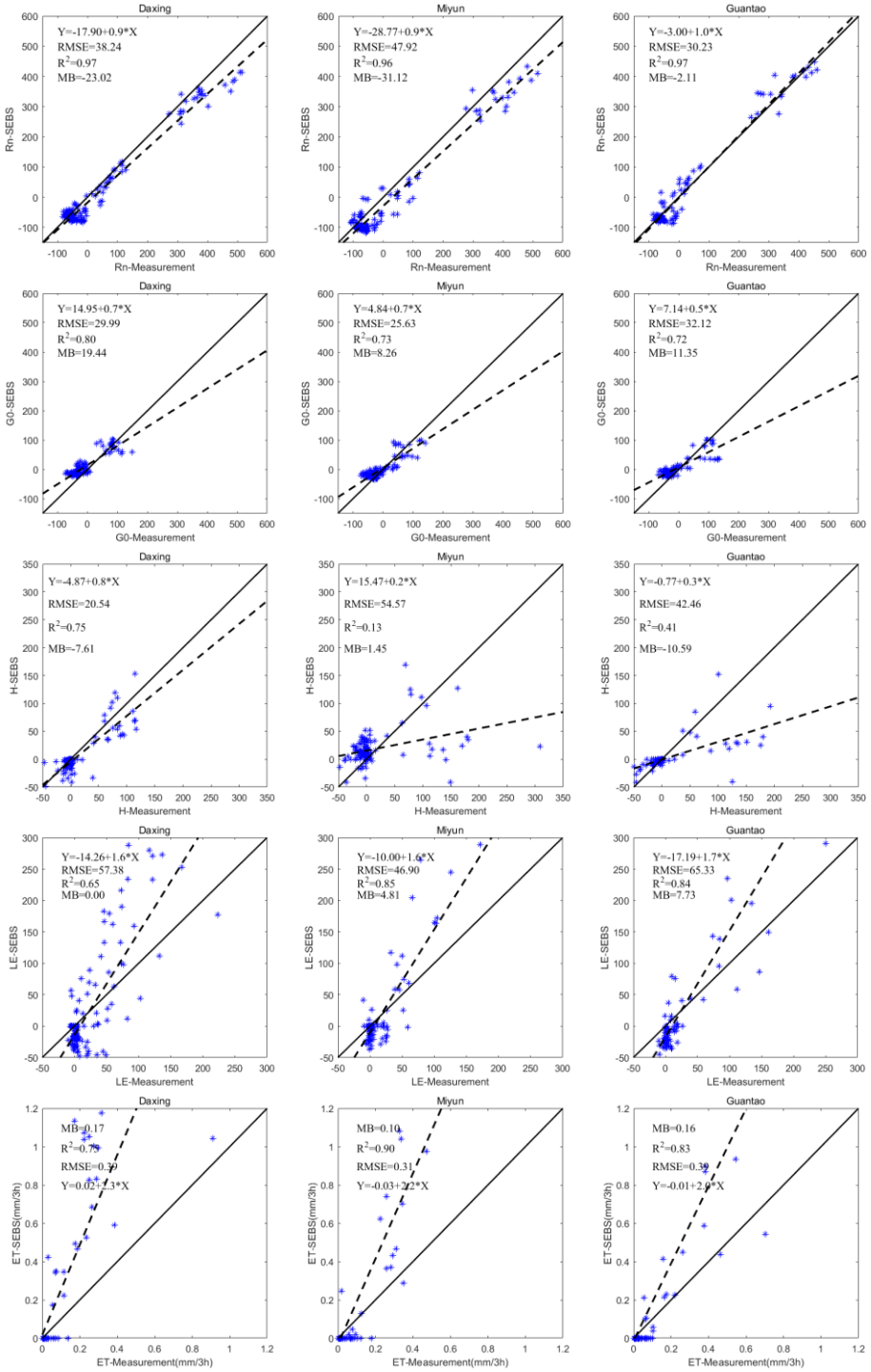
Daxing
Y=-17.90+0.9*X
RMSE=38.24
R2=0.97
MB=-23.02
Rn-SEBS
Rn-Measurement
Miyun
Y=-28.77+0.9*X
RMSE=47.92
R2=0.96
MB=-31.12
Rn-SEBS
Rn-Measurement
Guantao
Y=-3.00+1.0*X
RMSE=30.23
R2=0.97
MB=-2.11
Rn-SEBS
Rn-Measurement
Daxing
Y=14.95+0.7*X
RMSE=29.99
R2=0.80
MB=19.44
G0-SEBS
G0-Measurement
Miyun
Y=4.84+0.7*X
RMSE=25.63
R2=0.73
MB=8.26
G0-SEBS
G0-Measurement
Guantao
Y=7.14+0.5*X
RMSE=32.12
R2=0.72
MB=11.35
G0-SEBS
G0-Measurement
Daxing
Y=-4.87+0.8*X
RMSE=20.54
R2=0.75
MB=-7.61
H-SEBS
H-Measurement
Miyun
Y=15.47+0.2*X
RMSE=54.57
R2=0.13
MB=1.45
H-SEBS
H-Measurement
Guantao
Y=-0.77+0.3*X
RMSE=42.46
R2=0.41
MB=-10.59
H-SEBS
H-Measurement
Daxing
Y=-14.26+1.6*X
RMSE=57.38
R2=0.65
MB=0.00
LE-SEBS
LE-Measurement
Miyun
Y=-10.00+1.6*X
RMSE=46.90
R2=0.85
MB=4.81
LE-SEBS
LE-Measurement
Guantao
Y=-17.19+1.7*X
RMSE=65.33
R2=0.84
MB=7.73
LE-SEBS
LE-Measurement
Daxing
MB=0.17
R2=0.79
RMSE=0.39
Y=0.02+2.3*X
ET-SEBS(mm/3h)
ET-Measurement(mm/3h)
Miyun
MB=0.10
R2=0.90
RMSE=0.31
Y=-0.03+2.2*X
ET-SEBS(mm/3h)
ET-Measurement(mm/3h)
Guantao
MB=0.16
R2=0.83
RMSE=0.39
Y=-0.01+2.0*X
ET-SEBS(mm/3h)
ET-Measurement(mm/3h)

Test3

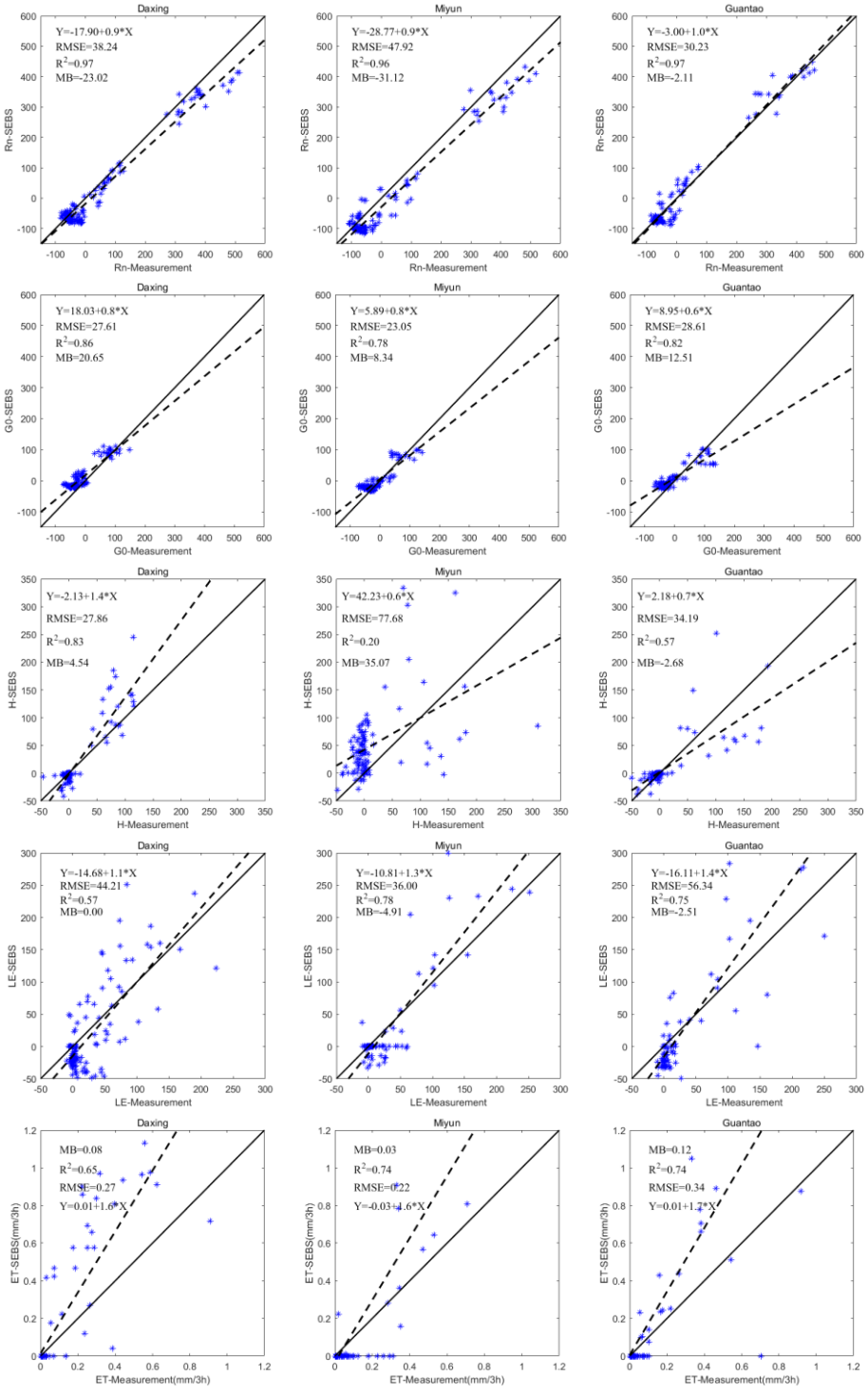
Daxing
Y=-17.90+0.9*X
RMSE=38.24
R2=0.97
MB=-23.02
Rn-SEBS
Rn-Measurement
Miyun
Y=-28.77+0.9*X
RMSE=47.92
R2=0.96
MB=-31.12
Rn-SEBS
Rn-Measurement
Guantao
Y=-3.00+1.0*X
RMSE=30.23
R2=0.97
MB=-2.11
Rn-SEBS
Rn-Measurement
Daxing
Y=18.03+0.8*X
RMSE=27.61
R2=0.86
MB=20.65
G0-SEBS
G0-Measurement
Miyun
Y=5.89+0.8*X
RMSE=23.05
R2=0.78
MB=8.34
G0-SEBS
G0-Measurement
Guantao
Y=8.95+0.6*X
RMSE=28.61
R2=0.82
MB=12.51
G0-SEBS
G0-Measurement
Daxing
Y=-2.13+1.4*X
RMSE=27.86
R2=0.83
MB=4.54
H-SEBS
H-Measurement
Miyun
Y=42.23+0.6*X
RMSE=77.68
R2=0.20
MB=35.07
H-SEBS
H-Measurement
Guantao
Y=2.18+0.7*X
RMSE=34.19
R2=0.57
MB=-2.68
H-SEBS
H-Measurement
Daxing
Y=-14.68+1.1*X
RMSE=44.21
R2=0.57
MB=0.00
LE-SEBS
LE-Measurement
Miyun
Y=-10.81+1.3*X
RMSE=36.00
R2=0.78
MB=-4.91
LE-SEBS
LE-Measurement
Guantao
Y=-16.11+1.4*X
RMSE=56.34
R2=0.75
MB=-2.51
LE-SEBS
LE-Measurement
Daxing
MB=0.08
R2=0.65
RMSE=0.27
Y=0.01+1.6*X
ET-SEBS(mm/3h)
ET-Measurement(mm/3h)
Miyun
MB=0.03
R2=0.74
RMSE=0.22
Y=-0.03+1.6*X
ET-SEBS(mm/3h)
ET-Measurement(mm/3h)
Guantao
MB=0.12
R2=0.74
RMSE=0.34
Y=0.01+1.2*X
ET-SEBS(mm/3h)
ET-Measurement(mm/3h)

Test4

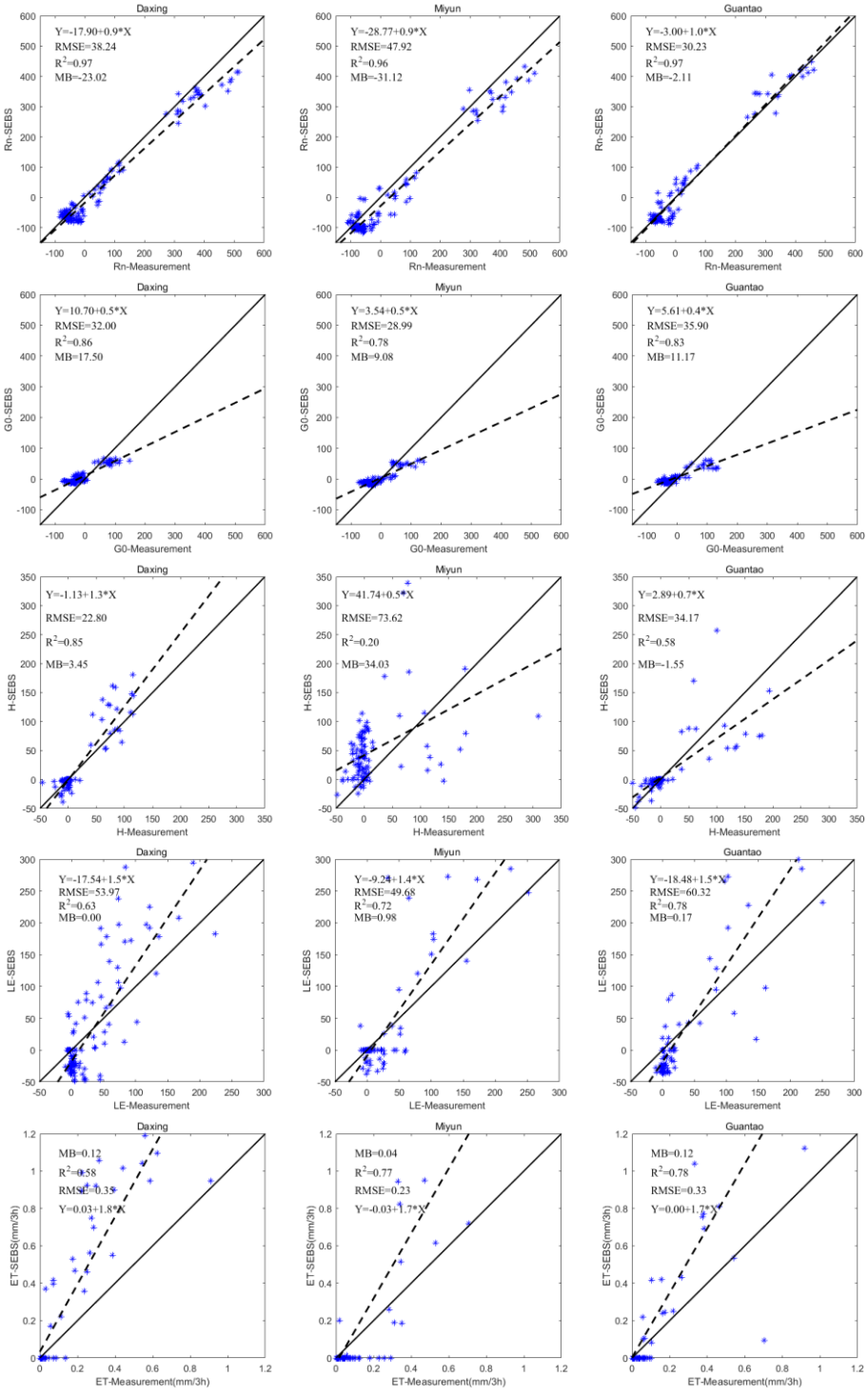
Daxing
Y=-17.90+0.9*X
RMSE=38.24
R2=0.97
MB=-23.02
Rn-SEBS
Rn-Measurement
Miyun
Y=-28.77+0.9*X
RMSE=47.92
R2=0.96
MB=-31.12
Rn-SEBS
Rn-Measurement
Guantao
Y=-3.00+1.0*X
RMSE=30.23
R2=0.97
MB=-2.11
Rn-SEBS
Rn-Measurement
Daxing
Y=10.70+0.5*X
RMSE=32.00
R2=0.86
MB=17.50
G0-SEBS
G0-Measurement
Miyun
Y=3.54+0.5*X
RMSE=28.99
R2=0.78
MB=9.08
G0-SEBS
G0-Measurement
Guantao
Y=5.61+0.4*X
RMSE=35.90
R2=0.83
MB=11.17
G0-SEBS
G0-Measurement
Daxing
Y=-1.13+1.3*X
RMSE=22.80
R2=0.85
MB=3.45
H-SEBS
H-Measurement
Miyun
Y=41.74+0.5*X
RMSE=73.62
R2=0.20
MB=34.03
H-SEBS
H-Measurement
Guantao
Y=2.89+0.7*X
RMSE=34.17
R2=0.58
MB=-1.55
H-SEBS
H-Measurement
Daxing
Y=-17.54+1.5*X
RMSE=53.97
R2=0.63
MB=0.00
LE-SEBS
LE-Measurement
Miyun
Y=-9.24+1.4*X
RMSE=49.68
R2=0.72
MB=0.98
LE-SEBS
LE-Measurement
Guantao
Y=-18.48+1.5*X
RMSE=60.32
R2=0.78
MB=0.17
LE-SEBS
LE-Measurement
Daxing
MB=0.12
R2=0.58
RMSE=0.35
Y=0.03+1.8*X
ET-SEBS(mm/3h)
ET-Measurement(mm/3h)
Miyun
MB=0.04
R2=0.77
RMSE=0.23
Y=-0.03+1.7*X
ET-SEBS(mm/3h)
ET-Measurement(mm/3h)
Guantao
MB=0.12
R2=0.78
RMSE=0.33
Y=0.00+1.7*X
ET-SEBS(mm/3h)
ET-Measurement(mm/3h)